How to cite: *Angew. Chem. Int. Ed.* **2021**, *60*, 17198–17204
International Edition: doi.org/10.1002/anie.202106769
German Edition: doi.org/10.1002/ange.202106769

Gas Separation **Hot Paper**

Optimal Pore Chemistry in an Ultramicroporous Metal–Organic Framework for Benchmark Inverse CO_2/C_2H_2 Separation

*Zhaoqiang Zhang, Shing Bo Peh, Rajamani Krishna, Chengjun Kang, Kungang Chai, Yuxiang Wang, Dongchen Shi, and Dan Zhao**

Abstract: *Isolation of CO_2 from acetylene (C_2H_2) via CO_2-selective sorbents is an energy-efficient technology for C_2H_2 purification, but a strategic challenge due to their similar physicochemical properties. There is still no specific methodology for constructing sorbents that preferentially trap CO_2 over C_2H_2. We report an effective strategy to construct optimal pore chemistry in a Ce^{IV}-based ultramicroporous metal–organic framework Ce^{IV}-MIL-140-4F, based on charge-transfer effects, for efficient inverse CO_2/C_2H_2 separation. The ligand-to-metal cluster charge transfer is facilitated by Ce^{IV} with low-lying unoccupied 4f orbitals and electron-withdrawing F atoms functionalized tetrafluoroterephthalate, affording a perfect pore environment to match CO_2. The exceptional CO_2 uptake (151.7 $cm^3 cm^{-3}$) along with remarkable separation selectivities (above 40) set a new benchmark for inverse CO_2/C_2H_2 separation, which is verified via simulated and experimental breakthrough experiments. The unique CO_2 recognition mechanism is further unveiled by in situ powder X-ray diffraction experiments, Fourier-transform infrared spectroscopy measurements, and molecular calculations.*

Introduction

Acetylene (C_2H_2) is one of the predominant precursor chemicals. It is mainly produced by partial combustion of natural gas and steam cracking of hydrocarbons, with a significant contaminant of CO_2 unavoidably co-generated.[1] Therefore, the separation of CO_2 from C_2H_2 is essential in the petrochemical industry to obtain high-purity C_2H_2. However, both C_2H_2 and CO_2 are non-polar. They have very similar physicochemical properties (boiling points of 189.3 and 194.7 K for C_2H_2 and CO_2, respectively) and almost identical size and dimension (kinetic diameter of 3.3 Å for both gases; $3.3\times3.3\times5.7$ Å^3 for C_2H_2 and $3.2\times3.3\times5.4$ Å^3 for CO_2; Supporting Information, Figure S1), undoubtedly giving rise to a daunting challenge for their separation.[1a–d] The CO_2/C_2H_2 separation process is implemented primarily by energy-intensive approaches, such as solvent extraction and cryogenic distillation. Adsorptive separation using porous adsorbents is a promising alternative technology, which is more environmentally friendly and energy-efficient than the heat-driven processes. However, the close similarities and the strict upper compression limit of C_2H_2 (2 bar) handicap the utilization of conventional porous materials, such as zeolites and carbon materials, for CO_2/C_2H_2 separation.[2] Thus, the development of novel porous materials for the efficient isolation of CO_2 from C_2H_2 is highly urgent yet challenging.

Metal–organic frameworks (MOFs) or porous coordination polymers (PCPs), self-assembled by inorganic metal nodes or clusters with organic ligands, have emerged as a new class of crystalline porous materials,[3] and offered a unique platform for addressing the challenges of gas separation.[4] Judicious design of the pore size/shape and pore chemistry by the modular nature of MOFs based on crystal engineering and reticular chemistry endows some MOFs with unprecedented adsorption and separation behaviors for light hydrocarbons, including C_2H_2/C_2H_4, C_3H_6/C_3H_8, C4 olefins, etc.[4,5] The almost identical molecular size of CO_2 and C_2H_2 renders it impractical and quite challenging for MOFs to discriminate them via fine-tuned pore size or shape. Numerous MOFs have been reported with substantial C_2H_2/CO_2 selectivity.[1c] This is due to the ease of designing active sites in MOFs for extra interactions with guests, such as acid-base interaction and hydrogen-bonding interaction. In the context of C_2H_2 and CO_2 separation, the acidic H atoms with positive charge in C_2H_2 are capable of interacting strongly with these active sites, resulting in high C_2H_2/CO_2 selectivity.[6] However, since CO_2 is the main contaminant in C_2H_2 (3% and even up to 50%),[2e] CO_2-selective sorbents are preferred for C_2H_2 purification because they will permit the direct isolation of C_2H_2 as a pure raffinate product. This will also efficiently leverage extensive industrial expertise in light-product-focused adsorptive cycles.[1c,2c] Unfortunately, MOFs exhibiting inverse CO_2/C_2H_2 selectivity are rare, and within this subset of materials, the trade-off between CO_2 adsorption capacity and inverse CO_2/C_2H_2 selectivity is still a significant barrier in prevailing materials. For example, SIFSIX-3-Ni,[1d] CD-MOFs,[7] and ionic crystals[8] with CO_2 uptake capacities of 98.4, 60.4, and 27 $cm^3 cm^{-3}$ only exhibit CO_2/C_2H_2 (1/2) selectivity of 7.7, 6.6, and 4.8, respectively. Thus, novel MOFs with high CO_2 capacity and inverse CO_2/C_2H_2 separation selectivity are of paramount importance in C_2H_2 purification. However, seeking strategies to construct MOFs with preferential sorption of CO_2 over C_2H_2 is still in its infancy.

---

[*] Dr. Z. Zhang, S. B. Peh, Dr. C. Kang, Prof. K. Chai, Dr. Y. Wang, D. Shi, Prof. D. Zhao
Department of Chemical and Biomolecular Engineering
National University of Singapore
4 Engineering Drive 4, 117585 Singapore (Singapore)
E-mail: chezhao@nus.edu.sg
Prof. R. Krishna
Van't Hoff Institute for Molecular Sciences, University of Amsterdam
Science Park 904, 1098 XH Amsterdam (The Netherlands)

Supporting information and the ORCID identification number(s) for the author(s) of this article can be found under: https://doi.org/10.1002/anie.202106769.

Notably, there is a huge difference in quadrupole moment between CO_2 (-13.4×10^{-40} C m^2)[9] and C_2H_2 ($+20.5\times10^{-40}$ C m^2, Figure S1),[2d,10] enlightening us to judiciously tune the pore chemistry with inverse electrostatic potential to leverage the quadrupole moment difference between CO_2 and C_2H_2, thus leading to inverse CO_2/C_2H_2 separation. For this reason, the metal node in MOFs should be in a high oxidation state to withdraw the electrons from ligands, producing a more polar pore surface to recognize CO_2 molecules preferentially. Accordingly, the strategy combining Ce^{IV} with unoccupied 4f orbitals and perfluorinated aromatic spacer, tetrafluoroterephthalate (TFBDC), meets such a request. Herein, we explored the framework, Ce^{IV}-MIL-140-4F, for inverse CO_2/C_2H_2 adsorption and separation, and compared its performance with the isostructural Zr^{IV}-MIL-140-4F, which is for the first time obtained and investigated. Notably, this pair of MOFs provides an interesting example of diverging sorption behaviors in isostructural frameworks, in which Ce^{IV}-MIL-140-4F exhibits excellent CO_2-preferential adsorption performance over C_2H_2, while Zr^{IV}-MIL-140-4F exhibits normal C_2H_2 selectivity over CO_2. Ce^{IV}-MIL-140-4F provides an optimal pore environment to match CO_2, and CO_2 is trapped into the pores via strong host-guest interactions by four F atoms from two linkers, which is evidenced by in situ powder X-ray diffraction (PXRD) and Fourier-transform infrared spectroscopy (FTIR) studies, as well as molecular simulations. As a result, Ce^{IV}-MIL-140-4F exhibits a superior CO_2 uptake of 151.7 $cm^3\,cm^{-3}$ at 273 K and excellent separation selectivities (above 40) for CO_2/C_2H_2 mixtures. In addition, breakthrough experiments and simulations further confirm the excellent CO_2/C_2H_2 separation performance. These results render Ce^{IV}-MIL-140-4F a new benchmark material for inverse CO_2/C_2H_2 separation, which is highly sought in the industrial separation process but rarely seen in the current literature.

Results and Discussion

The microcrystalline powder of Ce^{IV}-MIL-140-4F was obtained via refluxing cerium(IV) ammonium nitrate and H_2TFBDC in water at 383 K for 24 h.[11] Ce^{IV}-MIL-140-4F crystallizes in the monoclinic $C2/c$ space group and possesses perfluorinated one-dimensional triangular pore channels, making it highly hydrophobic (Figure S2). The Ce^{IV} ions in Ce^{IV}-MIL-140-4F exhibit a seven-coordination mode with three bridging μ_3-O oxygen atoms and four oxygen atoms from the dicarboxylic ligands, forming octahedral CeO_7 dimers. This is distinct from the 12-connected hexanuclear $Ce_6O_4(OH)_4(COO)_{12}$ clusters with structural hydroxy groups in the UiO-66 analogs.[11,12] The octahedra CeO_7 dimers are connected via the corner-sharing octahedra, leading to one-dimensional (1D) inorganic chains or sub-building units running along the c axis (Figure 1 a). The 1D chains are connected through six TFBDC moieties in perpendicular directions, constructing 1D triangular channels with abundant F atoms stretching into the pores with pore apertures of 3.4–4.3 Å (Figure 1 b). This pore structure is different from that in MIL-47 with 1D lozenge-shaped channels. This is due to the different coordination number of Ce^{IV} (7) compared to V^{V} (6), and the presence of a complex "double chain" inorganic building units in Ce^{IV}-MIL-140-4F (Figure 1 a) instead of a simple chain of corner-sharing octahedra in MIL-47.[13] Bulk purity of Ce^{IV}-MIL-140-4F was established by comparing experimental PXRD patterns with those calculated from crystal data (Figure 1 e). Replacing Ce^{IV} with Zr^{IV}, the perfluorinated analog Zr^{IV}-MIL-140-4F was obtained for the

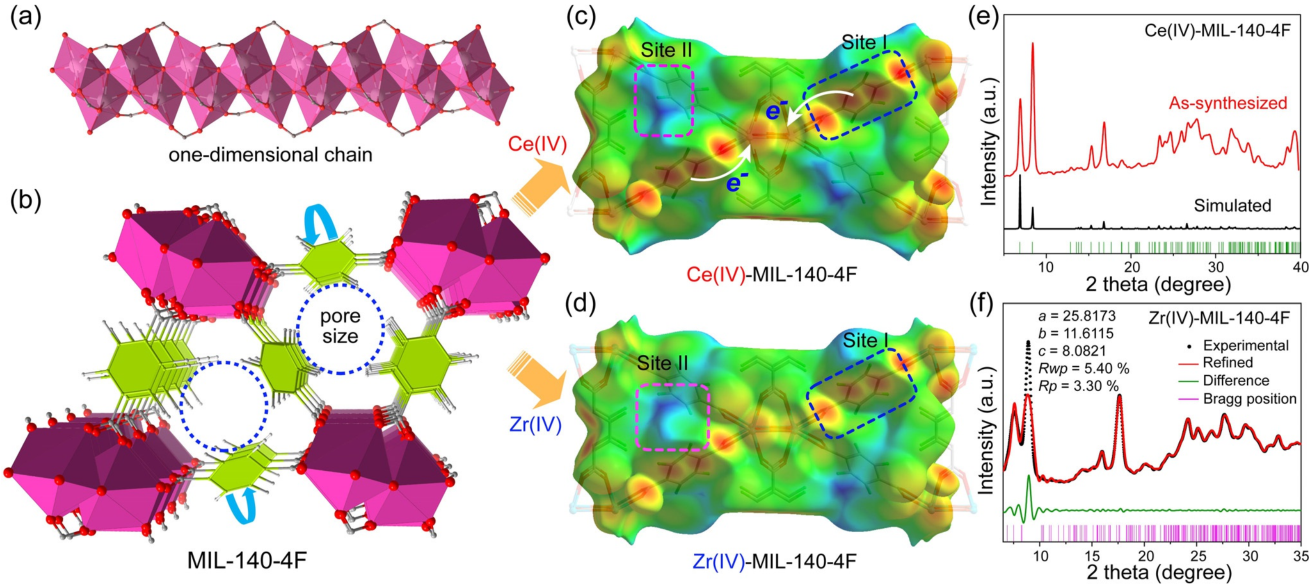

Figure 1. a) One-dimensional inorganic subunit of the metal oxide chain in MIL-140-14F. b) Illustration of the crystal structure and pore chemistry of MIL-140-4F. c,d) The Hirshfeld surface with d_e (electrostatic potential) and binding sites in Ce^{IV}- (c) and Zr^{IV}-MIL-140-4F (d) (red-to-blue color indicates the high-to-low transition of electron density). e) Experimental and simulated PXRD patterns of Ce^{IV}-MIL-140-4F. f) Experimental (black) and Pawley refined (red) PXRD patterns of Zr^{IV}-MIL-140-4F.

first time. The unit cell parameters ($a=25.8173$, $b=11.6115$, $c=8.0821$, $\alpha=\gamma=90$, $\beta=96.0813$) were confirmed via the Pawley refinement of the PXRD patterns in conjunction with structural of acceptable fitting metrics: $R_{wp}=5.4\,\%$ and $R_p=3.3\,\%$ (Figure 1 f; Supporting Information, Table S1). The unit cell of Ce^{IV}-MIL-140-4F is relatively smaller than that of Zr^{IV}-MIL-140-4F, as a consequence of the high oxidation state of Ce^{IV} with empty 4f orbitals facilitating the formation of a compact network.[11] To investigate the chemical properties of the channels and provide clues to the structure-property relationships, we analyzed the electrostatic potential distributions based on the Hirshfeld surface with d_e on MIL-140-4F materials (Figure 1 c,d).[14] The two MIL-140-4F MOFs exhibited a particular electronic distribution on their pore surface, with two distinct electronic regions in the edges of the triangular channels, denoted as electron-rich site I (blue dotted line) and electron-poor site II (pink dotted line). It is worth noting that Ce^{IV}-MIL-140-4F exhibits a much higher electron cloud density on site I and more positive potentials on site II, compared to Zr^{IV}-MIL-140-4F. This may originate from the strong electron-withdrawing effect of Ce^{IV} with empty and low-lying 4f orbitals facilitating ligand-to-cluster charge transfer, and this process can be accelerated by the functionalization of ligands with electron-withdrawing groups.[12a,c,d,15] Compared with the molecular properties of C_2H_2 and CO_2, it is expected that these two specific and distinct sites with inverse electron potential in MIL-140-4F can well match the inverse quadrupole moments of C_2H_2 and CO_2. Additionally, there is an obvious difference in pore electrostatic potential on site II between Ce^{IV}- and Zr^{IV}-MIL-140-4F, which means different host-guest interaction modes may be observed on site II for CO_2 and C_2H_2 adsorption.

Guest-free MIL-140-4F materials can be readily obtained at 100 °C in vacuo for 12 h, and thermogravimetric analyses demonstrated that Ce^{IV}-MIL-140-4F is thermally stable up to ca. 330 °C (Figure S3). Ce^{IV}-MIL-140-4F is chemically robust, being unaffected by soaking in water or exposing to air for prolonged periods, and even in strong acid solutions (1.6 mol L^{-1} of HNO_3), as confirmed by the PXRD patterns and CO_2 sorption isotherms (Figures S4 and S5). The permanent porosity of MIL-140-4F materials was confirmed by N_2 sorption experiments at 77 K. They exhibit fully reversible type-I isotherms without hysteresis, which is characteristic of microporous materials with permanent microporosity (Figure S6). The Brunauer-Emmett-Teller (BET) surface area and pore volume of Ce^{IV}-MIL-140-4F were calculated to be 360 m^2 g^{-1} and 0.11 cm^3 g^{-1}, respectively, relatively larger than that of Zr^{IV}-MIL-140-4F (314 m^2 g^{-1} and 0.11 cm^3 g^{-1}, respectively). All the values of pore size (Figure S7), volume, and surface area of MIL-140-4F materials are smaller than those of the UiO series (Figure S6) due to the simple 1D pore systems of MIL-140.

Considering the unique pore chemistry associated with suitable pore aperture size, low-pressure CO_2 and C_2H_2 sorption isotherms of Ce^{IV}- and Zr^{IV}-MIL-140-4F were collected and a marked difference in the sorption behavior for CO_2 and C_2H_2 was observed (Figure 2 a). Intriguingly, Ce^{IV}-MIL-140-4F exhibits an inverse CO_2-selective sorption behavior over C_2H_2. On the contrary, Zr^{IV}-MIL-140-4F preferentially adsorbs C_2H_2 over CO_2. Due to the industrial emphasis on the volume rather than the weight of the adsorbent in stationary applications, the volumetric capacity is often a better indicator of gas uptakes.[16] The CO_2 uptake of Ce^{IV}-MIL-140-4F is 110.3 cm^3 cm^{-3} at 298 K, much higher than that of C_2H_2 (41.5 cm^3 cm^{-3}), giving rise to a CO_2/C_2H_2 uptake ratio of 2.66. At 273 K, CO_2 and C_2H_2 uptakes can reach 151.7 and 53.5 cm^3 cm^{-3}, respectively (Figure 2 b). The uptake of CO_2 at 298 K is much higher than that of the most state-of-the-art CO_2-selective materials, such as MUF-16 (74.7 cm^3 cm^{-3}),[2c] SIFSIX-3-Ni (98.4 cm^3 cm^{-3}),[1d] PCP-NH$_2$-ipa (93.6 cm^3 cm^{-3}),[17] and CD-MOFs (60.4 cm^3 cm^{-3}).[7] At 273 K, the uptake is comparable with that of the benchmark Tm-OH-bdc (153 cm^3 cm^{-3})[18] (Figure 2 c), suggesting the feasibility of Ce^{IV}-MIL-140-4F in inverse CO_2/C_2H_2 separation. Notably, detailed analysis shows that the CO_2 isotherm of Ce^{IV}-MIL-140-4F exhibits a stepwise-shaped profile, indicating its flexibility, which may come from the rotation of benzene rings upon CO_2 sorption.[1a] The steep CO_2 isotherm at 273 K and the attainment of the plateau at low pressures indicate the strong affinity of the framework toward CO_2. Additionally, the 196 K isotherms of CO_2 and C_2H_2 further confirm the preferential adsorption performance of Ce^{IV}-MIL-140-4F for CO_2 over C_2H_2 (Figure 2 d). In contrast, Zr^{IV}-MIL-140-4F preferentially adsorbs C_2H_2 over CO_2, with uptakes of 95.7 and 48.6 cm^3 cm^{-3}, respectively, leading to a C_2H_2/CO_2 uptake ratio of 1.97 (Figure 2 a; Figure S10). Such inverse adsorption behaviors of Ce^{IV}- and Zr^{IV}-MIL-140-4F toward CO_2 and C_2H_2 are for the first time observed on two isostructural materials differing only in the composition of the metal nodes. To further investigate this behavior, we compared the analogous Ce-/Zr-UiO-66-4F materials-derived from the same metal-ligand combination under different synthetic conditions-with MIL-140 materials (Figure 2 e; Figures S10–S13). The results demonstrated that only Ce^{IV}-MIL-140-4F presents the inverse CO_2/C_2H_2 adsorption behavior.

To assess the separation potential of Ce^{IV}-MIL-140-4F for CO_2/C_2H_2 mixtures, ideal adsorbed solution theory (IAST) was applied to quantitatively evaluate the separation selectivity (Figures S15 and S16). Ce^{IV}-MIL-140-4F exhibits an excellent inverse CO_2/C_2H_2 (1/2) selectivity of up to 9.5 at 298 K. At 273 K, the selectivity can reach 41.5, much higher than that of the benchmark materials, such as Tm-OH-bdc (17.5 at 298 K),[18] CD-MOF-1 (6.6 at 298 K),[7] Mn(bdc)(bpe) (9.0 at 273 K),[8] and SIFSIX-3-Ni (7.7 at 298 K).[1d] High separation selectivity was also observed in Ce^{IV}-MIL-140-4F for CO_2/C_2H_2 (1/1) mixture, indicating promising separation potential for CO_2/C_2H_2 mixtures (Figure 2 c). The high separation selectivity for CO_2/C_2H_2 mixtures accompanied with high CO_2 volumetric capacity suggest Ce^{IV}-MIL-140-4F as a new benchmark for inverse CO_2/C_2H_2 separation. Furthermore, the coverage-dependent isosteric heats (Q_{st}) of adsorption for CO_2 on Ce^{IV}-MIL-140-4F was calculated to be 39.5 kJ mol^{-1} at zero coverage, remarkably higher than that of C_2H_2 (27.4 kJ mol^{-1}), presenting a stronger affinity to CO_2 over C_2H_2 (Figure S17). It is worth noting that the affinity for CO_2 is still moderate compared to other CO_2-preferential MOFs, such as Tm-OH-bdc (45.2 kJ mol^{-1}),[18] SIFSIX-3-Ni

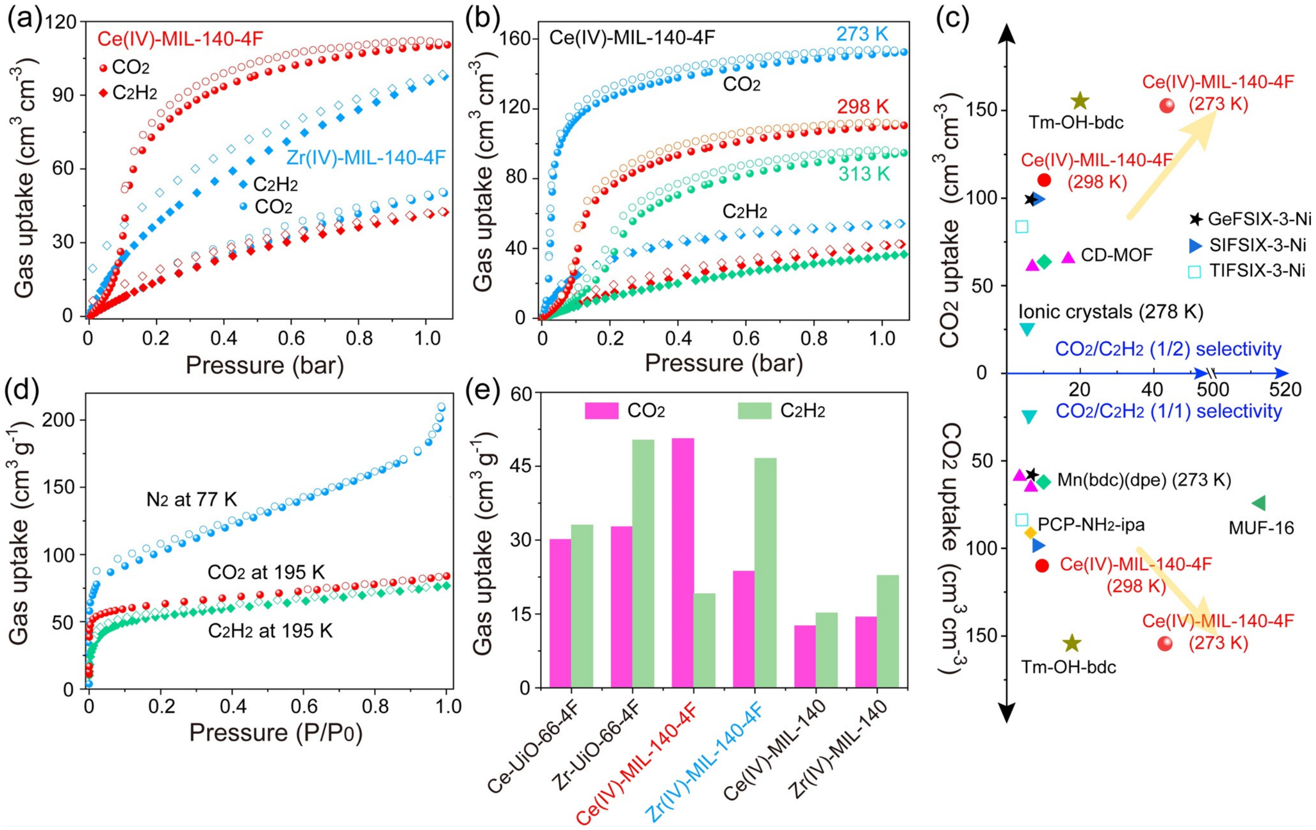

Figure 2. a) CO_2 and C_2H_2 isotherms of Ce^{IV}- and Zr^{IV}-MIL-140-4F collected at 298 K. b) CO_2 and C_2H_2 isotherms of Ce^{IV}-MIL-140-4F collected at different temperatures. c) Comparison of the best-performing materials for CO_2/C_2H_2 separation. d) CO_2 and C_2H_2 isotherms at 195 K and N_2 isotherm at 77 K of Ce^{IV}-MIL-140-4F. e) CO_2 and C_2H_2 uptakes of different materials at 298 K.

(50.9 kJ mol^{-1}),[1d] and CD-MOF-2 (67.2 kJ mol^{-1}).[7] Such a low Q_{st} value suggests facile regeneration of Ce^{IV}-MIL-140-4F under mild conditions in the CO_2/C_2H_2 separation process.

To gain deep insights into such anomalous CO_2-preferential adsorption performance, in situ PXRD measurement was carried out on CO_2-loaded Ce^{IV}-MIL-140-4F. The resolved structure shows that CO_2 is perfectly located on **site I** and bound by four F atoms coming from two parallel TFBDC ligands with F···C=O distances of 2.3 and 3.3 Å, respectively, indicating strong host-guest interactions (Figure 3a–c). Notably, the distance between two F atoms from two ligands in Figure 3c becomes 5.0 Å from the initial 4.9 Å, indicating a slight rotation of benzene rings upon CO_2 adsorption. This is consistent with the stepwise adsorption isotherms. To further investigate the host-guest interaction, in situ FTIR spectra on CO_2-loaded materials were collected (Figure 3d; Figures S20–S23). Interestingly, several new peaks at around 1000 and 1700 cm^{-1} were observed on CO_2-loaded Ce^{IV}-MIL-140-4F in comparison with the activated and CO_2-free sample, which may be due to the strong interactions between CO_2 and F atoms leading to the vibration and stretching of C-F bonds in TFBDC linker. However, in other materials such as Zr^{IV}-MIL-140-4F, Ce^{IV}-MIL-140, Ce-UiO-66-4F, and Zr^{IV}-MIL-140, no new peaks at around 1700 and 1000 cm^{-1} could be observed (Figures S20–S23), further consolidating the specific CO_2-preferential sorption performance of Ce^{IV}-MIL-140-4F. Additionally, two peaks at 444 and 790 cm^{-1} disappeared upon CO_2 loading, which may be due to the strong interactions between CO_2 and the framework. In contrast, DFT calculations for C_2H_2 in Ce^{IV}-MIL-140-4F indicate that C_2H_2 is located on **site II** with longer ≡C−H···F distances of 2.7–3.1 Å (Figure 3e) compared to the distances between CO_2 and the framework (2.3 Å), indicating the weaker binding affinity of the framework with C_2H_2. The special binding configurations of CO_2 and C_2H_2 in Ce^{IV}-MIL-14-4F demonstrate the efficiency of the constructive strategy for CO_2-selective sorbents. A similar binding mode for C_2H_2 on **site II** was observed in Zr^{IV}-MIL-140-4F with distances of 2.7–3.1 Å. Furthermore, the host-guest interaction between C_2H_2 and Zr^{IV}-MIL-140-4F was consolidated by the π···π interaction between benzene ring on TFBDC and the triple bond on C_2H_2 (3.3 Å, Figure 3 f). Similarly, CO_2 also located on **site II** with distances of 2.8–3.2 Å, shorter than that of C_2H_2, and no interactions between benzene rings and CO_2 were observed (Figure S24). The binding energy of Zr^{IV}-MIL-140-4F for C_2H_2 predicated by DFT calculations is 39.5 kJ mol^{-1}, higher than that of CO_2 (33.1 kJ mol^{-1}). This is consistent with the adsorption isotherms that Zr-MIL-140-4F exhibits the preferential adsorption ability for C_2H_2 over CO_2.

To evaluate the feasibility of Ce^{IV}-MIL-140-4F for selective inverse CO_2/C_2H_2 separation, transient breakthrough simulations were performed in fixed-bed adsorption processes.[19] The results show that highly efficient separations can be

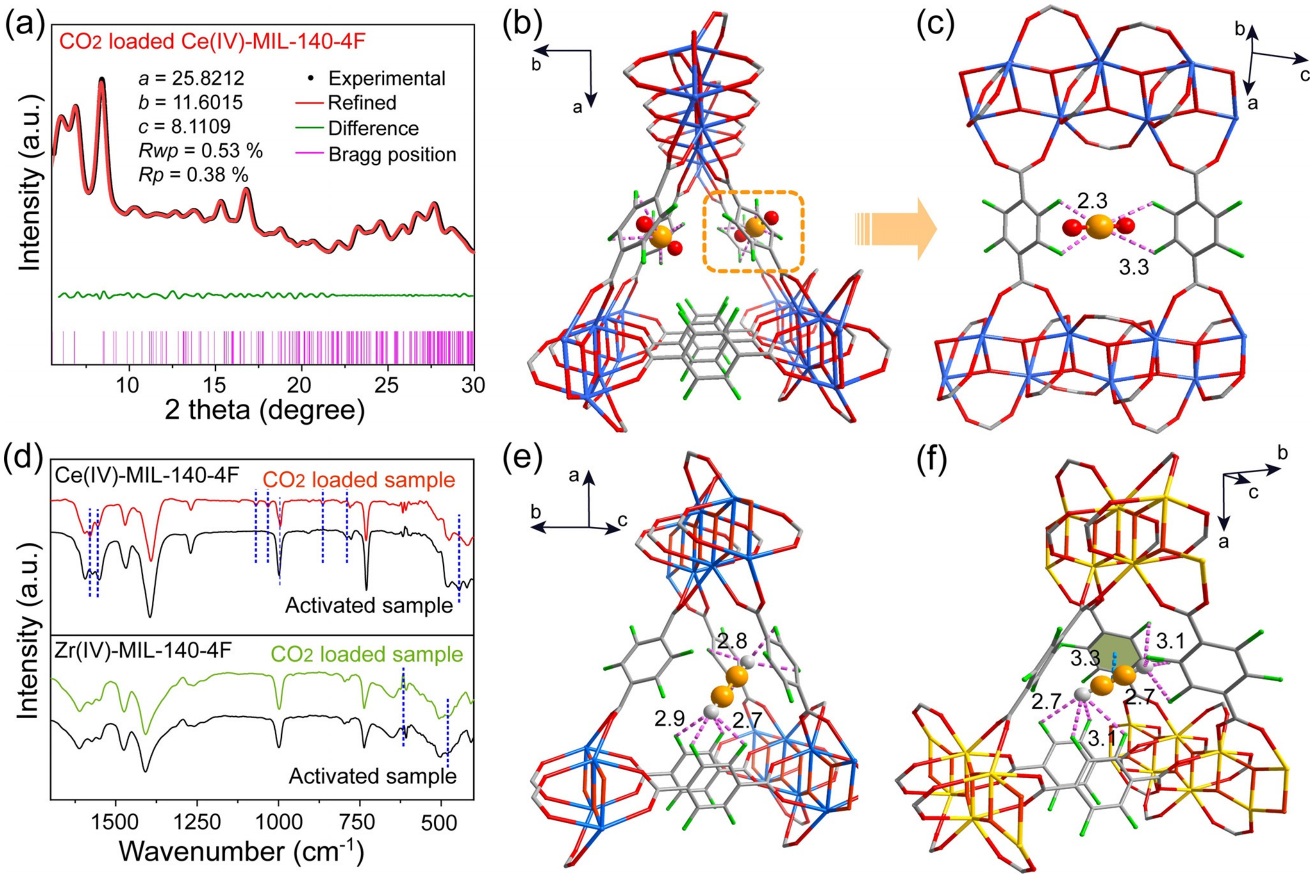

Figure 3. a) Experimental in situ and refined PXRD patterns of CO_2-loaded Ce^{IV}-MIL-140-4F. b,c) Refined structure of CO_2-loaded Ce^{IV}-MIL-140-4F with CO_2 strongly bound by four F atoms. d) In situ FTIR spectra of the activated and CO_2-loaded Ce^{IV}- and Zr^{IV}-MIL-140-4F. e) The binding site of C_2H_2 in Ce^{IV}-MIL-140-4F. f) The DFT-calculated binding configuration of C_2H_2 in Zr^{IV}-MIL-140-4F.

accomplished by Ce^{IV}-MIL-140-4F for CO_2/C_2H_2 (1/1 and 1/2) mixtures at 273 and 298 K, with high-purity C_2H_2 harvested via a one-step breakthrough experiment (Figure 4a; Figure S25a). The calculated productivity of high-purity C_2H_2 (> 99 %) can reach 132.2 and 66.6 $m^3 L^{-1}$ at 273 K and 298 K, respectively, much higher than that on PCP-NH$_2$-ipa (28.5 $m^3 L^{-1}$).[17] We further carried out the experimental breakthrough studies with CO_2/C_2H_2 (1/1 and 1/2) mixtures flowed over a Ce^{IV}-MIL-140-4F-packed column at 273 and 298 K (Figure 4b; Figure S25b). A clear separation of CO_2/C_2H_2 mixtures was realized, which is consistent with the simulated breakthrough results. C_2H_2 eluted through the column first to yield an outflow of pure C_2H_2 (> 99.99 %) with an undetectable amount of CO_2 in a single breakthrough operation. Notably, this is difficult for C_2H_2-selective adsorbents in the desorption process due to the co-adsorption of C_2H_2 and CO_2. Furthermore, CO_2 can be efficiently retained in the column for long periods with the dynamic capture

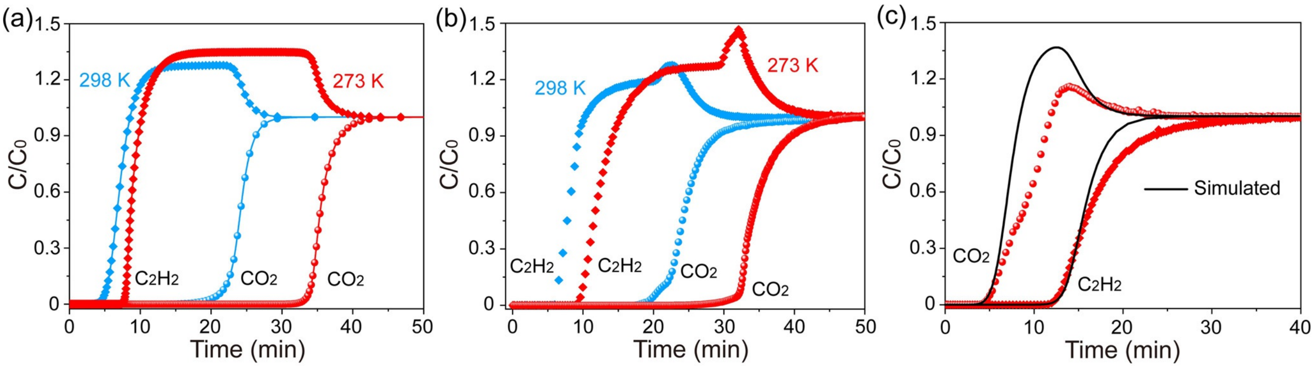

Figure 4. a) Simulated and b) experimental breakthrough curves for CO_2/C_2H_2 (1/1) separation in a fixed bed packed with Ce^{IV}-MIL-140-4F at 273 and 298 K. c) Simulated and experimental breakthrough curves of C_2H_2/CO_2 (1/1) mixture on Zr^{IV}-MIL-140-4F at 298 K. All the simulated and experimental breakthrough curves were investigated at 1 bar with a flow rate of 2 mL min^{-1}.

amounts of 136.9 and 99.7 $cm^3 cm^{-3}$ at 273 and 298 K, respectively. Such a high working capacity is coincident with the CO_2 adsorption isotherms. Moreover, the CO_2/C_2H_2 separation performance was unimpeded by humidity (Figure S26), which may be due to the hydrophobic pore channels. The remarkable roll-up phenomenon on C_2H_2 curves indicates strong competitive sorption of CO_2 over C_2H_2 on Ce^{IV}-MIL-140-4F. The separation factors for CO_2/C_2H_2 (1/1) mixtures calculated from breakthrough experiments are 4.9 and 5.6 at 298 and 273 K, respectively. In contrast, Zr^{IV}-MIL-140-4F exhibits good separation performance for C_2H_2/CO_2 mixtures (Figure 4c). Last but not least, the cycle and regeneration capabilities of Ce^{IV}-MIL-140-4F were investigated (Figures S27 and S28). The results show that the column can be simply regenerated by purging He at room temperature. The inverse CO_2/C_2H_2 separation capability of Ce^{IV}-MIL-140-4F was well retained with no noticeable decrease observed, confirming its good stability for inverse CO_2/C_2H_2 separation. The above results demonstrate that Ce^{IV}-MIL-140-4F can be a promising adsorbent for inverse CO_2/C_2H_2 separation with desirable high-purity C_2H_2 obtained via a single separation operation.

Conclusion

In summary, we judiciously realized the efficient inverse CO_2/C_2H_2 adsorption and separation with an ultramicroporous Ce^{IV}-based MOF, Ce^{IV}-MIL-140-4F. Owing to the unoccupied 4f orbitals of Ce^{IV} with a strong electron-withdrawing effect from the fluorinated linkers, Ce^{IV}-MIL-140-4F exhibits optimal pore chemistry of negative electrostatic potential around four F atoms coming from two parallel linkers. This optimal pore environment can preferentially trap CO_2 through the strong F···C=O interactions. On the contrary, Zr^{IV}-MIL-140-4F only shows a normal C_2H_2/CO_2 separation selectivity. The inverse CO_2-selective sorption behavior of Ce^{IV}-MIL-140-4F was revealed by in situ PXRD and FTIR experiments, as well as molecular calculations. Such unique pore chemistry endows Ce^{IV}-MIL-140-4F with benchmark inverse CO_2/C_2H_2 separation performance. High-purity C_2H_2 (> 99.99 %) can be directly obtained from CO_2/C_2H_2 mixtures through a single adsorption procedure, which was confirmed by the detailed simulated and experimental breakthrough studies. The elaborate design strategy for pore chemistry based on the intrinsic nature or differences between molecules is an effective way to control the discrimination ability of porous materials. This work opens a new avenue for the design of advanced porous materials in gas separation.

Acknowledgements

This work was supported by the National Research Foundation Singapore (NRF2018-NRF-ANR007 POCEMON), the Ministry of Education-Singapore (MOE AcRF Tier 2 MOE2018-T2-2-148, MOE2019-T2-1-093), and the Agency for Science, Technology and Research (IRG A1783c0015, IAF-PP A1789a0024).

Conflict of Interest

The authors declare no conflict of interest.

Keywords: CO_2/C_2H_2 separation · inverse adsorption and separation · pore chemistry · quadrupole moments · ultramicroporous MOFs

---

[1] a) M. L. Foo, R. Matsuda, Y. Hijikata, R. Krishna, H. Sato, S. Horike, A. Hori, J. Duan, Y. Sato, Y. Kubota, M. Takata, S. Kitagawa, *J. Am. Chem. Soc.* **2016**, *138*, 3022–3030; b) R. B. Lin, L. Li, H. Wu, H. Arman, B. Li, R. G. Lin, W. Zhou, B. Chen, *J. Am. Chem. Soc.* **2017**, *139*, 8022–8028; c) S. Mukherjee, D. Sensharma, K. J. Chen, M. J. Zaworotko, *Chem. Commun.* **2020**, *56*, 10419–10441; d) K. J. Chen, H. S. Scott, D. G. Madden, T. Pham, A. Kumar, A. Bajpai, M. Lusi, K. A. Forrest, B. Space, J. J. Perry, M. J. Zaworotko, *Chem* **2016**, *1*, 753–765; e) Y. Ye, Z. Ma, R. B. Lin, R. Krishna, W. Zhou, Q. Lin, Z. Zhang, S. Xiang, B. Chen, *J. Am. Chem. Soc.* **2019**, *141*, 4130–4136; f) J. Zhang, X. Chen, *J. Am. Chem. Soc.* **2009**, *131*, 5516–5521.

[2] a) R. Matsuda, R. Kitaura, S. Kitagawa, Y. Kubota, R. V. Belosludov, T. C. Kobayashi, H. Sakamoto, T. Chiba, M. Takata, Y. Kawazoe, Y. Mita, *Nature* **2005**, *436*, 238–241; b) J. Gao, X. Qian, R. B. Lin, R. Krishna, H. Wu, W. Zhou, B. Chen, *Angew. Chem. Int. Ed.* **2020**, *59*, 4396–4400; *Angew. Chem.* **2020**, *132*, 4426–4430; c) O. T. Qazvini, R. Babarao, S. G. Telfer, *Nat. Commun.* **2021**, *12*, 197; d) C. T. He, Z. M. Ye, Y. T. Xu, D. D. Zhou, H. L. Zhou, D. Chen, J. P. Zhang, X. M. Chen, *Chem. Sci.* **2017**, *8*, 7560–7565; e) S. Liu, X. Han, Y. Chai, G. Wu, W. Li, J. Li, I. da-Silva, P. Manuel, Y. Cheng, L. L. Daemen, A. J. Ramirez-Cuesta, W. Shi, N. Guan, S. Yang, L. Li, *Angew. Chem. Int. Ed.* **2021**, *60*, 6526–6532; *Angew. Chem.* **2021**, *133*, 6600–6606.

[3] a) A. Schoedel, M. Li, D. Li, M. O'Keeffe, O. M. Yaghi, *Chem. Rev.* **2016**, *116*, 12466–12535; b) Z. Ji, H. Wang, S. Canossa, S. Wuttke, O. M. Yaghi, *Adv. Funct. Mater.* **2020**, *30*, 2000238; c) M. O'Keeffe, O. M. Yaghi, *Chem. Rev.* **2012**, *112*, 675–702.

[4] a) J. R. Li, J. Sculley, H. C. Zhou, *Chem. Rev.* **2012**, *112*, 869–932; b) X. Zhao, Y. Wang, D. S. Li, X. Bu, P. Feng, *Adv. Mater.* **2018**, *30*, 1705189; c) H. Wang, Y. Liu, J. Li, *Adv. Mater.* **2020**, *32*, 2002603; d) B. R. Barnett, M. I. Gonzalez, J. R. Long, *Trends Chem.* **2019**, *1*, 159–171; e) K. Adil, Y. Belmabkhout, R. S. Pillai, A. Cadiau, P. M. Bhatt, A. H. Assen, G. Maurin, M. Eddaoudi, *Chem. Soc. Rev.* **2017**, *46*, 3402–3430; f) T. Islamoglu, Z. Chen, M. C. Wasson, C. T. Buru, K. O. Kirlikovali, U. Afrin, M. R. Mian, O. K. Farha, *Chem. Rev.* **2020**, *120*, 8130–8160; g) Z. Zhang, B. Tan, P. Wang, X. Cui, H. Xing, *AIChE J.* **2020**, *66*, e16236.

[5] a) Z. Zhang, S. B. Peh, Y. Wang, C. Kang, W. Fan, D. Zhao, *Angew. Chem. Int. Ed.* **2020**, *59*, 18927–18932; *Angew. Chem.* **2020**, *132*, 19089–19094; b) Z. Zhang, Q. Yang, X. Cui, L. Yang, Z. Bao, Q. Ren, H. Xing, *Angew. Chem. Int. Ed.* **2017**, *56*, 16282–16287; *Angew. Chem.* **2017**, *129*, 16500–16505; c) Q. Ding, Z. Zhang, C. Yu, P. Zhang, J. Wang, X. Cui, C. He, S. Deng, H. Xing, *Sci. Adv.* **2020**, *6*, eaaz4322; d) Z. Zhang, Q. Ding, J. Cui, X. Cui, H. Xing, *Small* **2020**, *16*, 2005360.

[6] a) Y. Du, Y. Chen, Y. Wang, C. He, J. Yang, L. Li, J. Li, *Sep. Purif. Technol.* **2021**, *256*, 117749; b) Y. L. Peng, T. Pham, P. Li, T. Wang, Y. Chen, K. J. Chen, K. A. Forrest, B. Space, P. Cheng, M. J. Zaworotko, Z. Zhang, *Angew. Chem. Int. Ed.* **2018**, *57*, 10971–10975; *Angew. Chem.* **2018**, *130*, 11137–11141; c) J. Lee, C. Y. Chuah, J. Kim, Y. Kim, N. Ko, Y. Seo, K. Kim, T. H. Bae, E. Lee, *Angew. Chem. Int. Ed.* **2018**, *57*, 7869–7873; *Angew. Chem.* **2018**, *130*, 7995–7999; d) J. Pei, K. Shao, J. Wang, H. Wen, Y.

Yang, Y. Cui, R. Krishna, B. Li, G. Qiang, *Adv. Mater.* **2020**, *32*, 1908275.

[7] L. Li, J. Wang, Z. Zhang, Q. Yang, Y. Yang, B. Su, Z. Bao, Q. Ren, *ACS Appl. Mater. Interfaces* **2019**, *11*, 2543 – 2550.

[8] R. Eguchi, S. Uchida, N. Mizuno, *Angew. Chem. Int. Ed.* **2012**, *51*, 1635 – 1639; *Angew. Chem.* **2012**, *124*, 1667 – 1671.

[9] C. Graham, J. Pierrus, R. E. Raab, *Mol. Phys.* **1989**, *67*, 939 – 955.

[10] A. Halkier, S. Coriani, *Chem. Phys. Lett.* **1999**, *303*, 408 – 412.

[11] R. D'Amato, A. Donnadio, M. Carta, C. Sangregorio, D. Tiana, R. Vivani, M. Taddei, F. Costantino, *ACS Sustainable Chem. Eng.* **2019**, *7*, 394 – 402.

[12] a) J. Jacobsen, L. Wegner, H. Reinsch, N. Stock, *Dalton Trans.* **2020**, *49*, 11396 – 11402; b) M. Campanelli, T. Del Giacco, F. De Angelis, E. Mosconi, M. Taddei, F. Marmottini, R. D'Amato, F. Costantino, *ACS Appl. Mater. Interfaces* **2019**, *11*, 45031 – 45037; c) X. P. Wu, L. Gagliardi, D. G. Truhlar, *J. Chem. Phys.* **2019**, *150*, 041701; d) X. Wu, L. Gagliardi, D. Truhlar, *J. Am. Chem. Soc.* **2018**, *140*, 7904 – 7912.

[13] V. Guillerm, F. Ragon, M. Dan-Hardi, T. Devic, M. Vishnuvarthan, B. Campo, A. Vimont, G. Clet, Q. Yang, G. Maurin, G. Ferey, A. Vittadini, S. Gross, C. Serre, *Angew. Chem. Int. Ed.* **2012**, *51*, 9267 – 9271; *Angew. Chem.* **2012**, *124*, 9401 – 9405.

[14] Q. Zhang, M. Wahiduzzaman, S. Wang, S. Henfling, N. Ayoub, E. Gkaniatsou, F. Nouar, C. Sicard, C. Martineau, Y. Cui, G. Maurin, G. Qian, C. Serre, *Chem* **2019**, *5*, 1337 – 1350.

[15] a) E. Caballero-Mancebo, B. Cohen, S. Smolders, D. E. De Vos, A. Douhal, *Adv. Sci.* **2019**, *6*, 1901020; b) T. Islamoglu, A. Atilgan, S. Moon, G. W. Peterson, J. B. DeCoste, M. Hall, J. T. Hupp, O. K. Farha, *Chem. Mater.* **2017**, *29*, 2672 – 2675.

[16] Z. Hu, Y. Wang, B. Shah, D. Zhao, *Adv. Sustainable Syst.* **2019**, *3*, 1800080.

[17] Y. Gu, J. Zheng, K. Otake, M. Shivanna, S. Sakaki, H. Yoshino, M. Ohba, S. Kawaguchi, Y. Wang, F. Li, S. Kitagawa, *Angew. Chem. Int. Ed.* **2021**, *60*, 11688 – 11694; *Angew. Chem.* **2021**, *133*, 11794 – 11800.

[18] D. Ma, Z. Li, J. Zhu, Y. Zhou, L. Chen, X. Mai, M. Liufu, Y. Wu, Y. Li, *J. Mater. Chem. A* **2020**, *8*, 11933 – 11937.

[19] a) R. Krishna, *RSC Adv.* **2017**, *7*, 35724 – 35737; b) R. Krishna, *RSC Adv.* **2015**, *5*, 52269 – 52295; c) R. Krishna, *Microporous Mesoporous Mater.* **2014**, *185*, 30 – 50.

Manuscript received: May 20, 2021
Accepted manuscript online: May 27, 2021
Version of record online: June 29, 2021

Angewandte Chemie
Eine Zeitschrift der Gesellschaft Deutscher Chemiker

Supporting Information

Optimal Pore Chemistry in an Ultramicroporous Metal–Organic Framework for Benchmark Inverse CO_2/C_2H_2 Separation

*Zhaoqiang Zhang, Shing Bo Peh, Rajamani Krishna, Chengjun Kang, Kungang Chai, Yuxiang Wang, Dongchen Shi, and Dan Zhao**

anie_202106769_sm_miscellaneous_information.pdf
anie_202106769_sm_Movie_S1.mp4
anie_202106769_sm_Movie_S2.mp4
anie_202106769_sm_Movie_S3.mp4

Table of Contents

Experimental Procedures S3
Supplementary Figures S5
Supplementary Tables S19
Supplementary Movie Titles S24
References S25

Experimental Procedures

Synthesis of Ce(IV)- and Zr(IV)-MIL-140-4F

Ce(IV)-MIL-140-4F was synthesized according to the reported method.[1] A mixture of cerium ammonium nitrate ($(NH_4)_2Ce(NO_3)_6$, CAN, 0.548 g, 1 mmol) and tetrafluoroterephthalic acid (H_2TFBDC, 0.238 g, 1 mmol) in deionized (DI) water (50 mL) was heated to 110 °C under stirring and refluxed for 24 h. The obtained yellow solid was filtered and washed with water and acetone. The solid was then dried under vacuum at 80 °C for 24 h, resulting in Ce(IV)-MIL-140-4F. Differently, Zr(IV)-MIL-140-4F was achieved by refluxing the mixtures of zirconium tetrachloride ($ZrCl_4$, 0.233 g, 1 mmol) and H_2TFBDC (0.238 g, 1 mmol) in acetonitrile (50 mL) at 120 °C under stirring for 48 h. The resulted slurry was centrifuged and washed with acetone three times, then dried under vacuum at 120 °C for 24 h, leading to Zr(IV)-MIL-140-4F.

Synthesis of Ce-UiO-66-4F

Briefly, CAN (0.548 g, 1 mmol), H_2TFBDC (0.238 g, 1 mmol), and acetic acid (6 mL) were dissolved in DI water (45 mL) in a round-bottom flask. The solution was heated to 110 °C under stirring and refluxed for 24 h. The obtained yellow solid was collected and washed three times with DI water and once with acetone. The solid was then dried at 80 °C for 24 h, resulting in Ce-UiO-66-4F.

Synthesis of Zr(IV)-MIL-140

A mixture of 1,4-benzenedicarboxylic acid (H_2BDC, 0.332 g, 2 mmol), $ZrCl_4$ (0.233 g, 1 mmol), and DMF (8 mL) was gently stirred and introduced into a 25 mL Teflon-lined steel autoclave. The autoclave was sealed and placed in an oven at 220 °C and kept for 16 h. The white solid was then filtered and dried at 100 °C for 12 h, leading to Zr(IV)-MIL-140.

Synthesis of Ce(IV)-MIL-140

Briefly, CAN (0.274 g, 0.5 mmol) and H_2BDC (0.249 g, 0.75 mmol) were dissolved in acetonitrile (10 mL), then introduced into a microwave glass reactor (25 mL). The reactor was sealed and heated for 4 h at 140 °C. After cooling down to room temperature, the yellow product was filtered off, washed with acetone three times. The solid was then dried under vacuum at 100 °C for 12 h, resulting in Ce(IV)-MIL-140.

TGA measurements

Thermogravimetric analyses (TGA) were performed on TA Instruments STD-600 at a heating rate of 10 K min^{-1} up to 800 °C with an N_2 flow rate of 50 mL min^{-1}. The sample holders were alumina crucibles, and the amount of sample used in each measurement was 10 (± 2) mg. The data collected were analyzed using Universal Analysis software (version 4.4A) from TA Instruments.

Gas sorption experiments

Adsorption and desorption experiments of CO_2 and C_2H_2 were performed at different temperatures on a Micromeritics ASAP 2020 instrument equipped with commercial software for data calculation and analysis. The test temperatures were controlled by soaking the sample cell into a circulating water bath (298 K) or ice water bath (273 K). Before measurement, the sample (80–100 mg) was degassed at 373 K for 12 h. The gas isotherms were obtained under a pressure range of 0–100 kPa. CO_2 and N_2 isotherms at 196 K and 77 K, respectively, were also collected on a Micromeritics ASAP2020 instrument. The measurement temperatures were maintained at 195 and 77 K using dry ice/acetone and liquid nitrogen, respectively.

Powder X-ray diffraction analyses

Powder X-ray diffraction (PXRD) patterns were collected using a Rigaku Miniflex 600 diffractometer (Cu Kα λ = 1.540598 Å) with an operating power of 40 kV, 15 mA, and a scan rate of 2.0 ° min^{-1}. The data were collected in a two-theta range of 5–40°. In situ PXRD patterns were collected with a chamber holding the sample, which was firstly evacuated and then filled with CO_2 gas. Pawley refinement was performed on the obtained PXRD data using the Reflex Module in *Materials Studio* software. Due to the abundant atoms in the crystal unit cell, the ligand molecule and the gas molecule were both treated as rigid bodies during the Pawley refinements, with the molecule orientation and center of mass freely refined. Final refinement on the positions/orientations of the rigid bodies, thermal factors, occupancies, lattice parameters, background, and profiles converged with satisfactory *R*-factors.

In situ Fourier transform infrared spectroscopy

The *in situ* Fourier transform infrared (FTIR) spectra were recorded using an FTIR spectrometer (Bruker VERTEX 70-FTIR). Before each experiment, the sample (~100 mg) was pretreated under high vacuum conditions (< 3 μmHg) at 393 K for 6 h, and then cooled to room temperature. The sample was then exposed to CO_2 with a pressure of 1.0 bar for 24 h to ensure that the adsorption has reached equilibrium. Then the sample was used for FTIR measurements. All the spectra were recorded over accumulative 32 scans with a resolution of 4 cm^{-1} in the range of 4000–400 cm^{-1}.

Breakthrough experiments

The breakthrough experiments were performed using a home-built dynamic gas breakthrough setup. The experiment was conducted using a stainless-steel column (4.6 mm inner diameter × 50 mm length). Before the breakthrough experiment, the column packed with Ce(IV)- or Zr(IV)-MIL-140-4F (0.55 or 0.5 g, respectively) was firstly activated with a He flow (5 mL min^{-1}) at 423 K for 12 h. After activation, the gas mixture (C_2H_2/CO_2, volume ratio of 1/1 or 2/1) was introduced, and outlet gas from the column was monitored by a mass spectrometer (Hiden QGA quantitative gas analysis system). After the breakthrough experiment, the sample was regenerated with a He flow (5 mL min^{-1}) at 373 K. Before each cyclic experiment, the sample was activated by heating at 100 °C for 6 h.

Breakthrough simulations

Transient breakthrough simulations were performed using the simulation methodology described previously.[2] The breakthrough experiments were conducted in a tube of diameter d = 4.6 mm and length L = 0.05 m. The mass of the crystallites in the packed tube is m_{ads}. For a crystal framework density of ρ kg m^{-3}, we calculated $(1-\varepsilon)=\frac{\frac{m_{ads}}{\rho}}{\frac{\pi d^2 L}{4}}$ and $\varepsilon = 1-\frac{\frac{m_{ads}}{\rho}}{\frac{\pi d^2 L}{4}}$. The crystal framework densities of Ce(IV)-MIL-140-4F and Zr(IV)-MIL-140-4F are 2170 kg m^{-3} and 2050 kg m^{-3}, respectively. The total flow rate of the gas mixture at the entrance Q_0 = 2 mL min^{-1} = 3.333 × 10^{-8} m^3 s^{-1}. The superficial gas velocity at the inlet to the adsorber $u=\frac{Q_0}{\frac{\pi d^2}{4}}$. The interstitial velocity $v=\frac{Q_0}{\frac{\varepsilon \pi d^2}{4}}$. The breakthrough simulations were performed for a total gas pressure of 100 kPa, with a constant temperature of 273 or 298 K. During the initial transience, the effluent gas contains pure C_2H_2, and this continues until CO_2 starts breaking through because its uptake capacity in the MOF has been reached. During a certain interval, τ_{break}, pure C_2H_2 can be recovered in the gas phase. The desired purity level for C_2H_2 was set at say 99%+, then the number of moles of C_2H_2 purged during the time intervals 0 to τ_{break}, can be determined from a material balance. Dividing the purged number of moles of C_2H_2 by the mass of adsorbent in the bed, m_{ads}, yields the productivity of C_2H_2 (mol kg^{-1}). The gravimetric CO_2 uptake capacity, expressed in mol kg^{-1}, can be determined from a material balance.

DFT calculations

First-principles density functional theory (DFT) calculations were performed in Castep software (*BIOVIA Materials Studio*).[3] A semi-empirical addition of dispersive forces to conventional DFT was included in the calculation to account for van der Waals interactions. Vanderbilt-type ultra-soft pseudopotentials and generalized gradient approximation with Perdew–Burke–Ernzerhof exchange correlation were used. A cutoff energy of 590 eV and a 1 × 1 × 2 *k*-point mesh (generated using the Monkhorst-Pack scheme) were found to be enough for the total energy to converge within 0.01 meV atom^{-1}. The structures of the synthesized materials were firstly optimized, then various guest gas molecules were introduced to various locations of the channel pore, followed by a full structural relaxation. To obtain the gas binding energy, an isolated gas molecule placed in a supercell (with the same cell dimensions as the material crystal) was also relaxed as a reference. The static binding energy (at T = 0 K) was then calculated using: $E_B = E_{(MOF)} + E_{(gas)} - E_{(MOF+gas)}$.

IAST selectivity calculations

The isotherm data for CO_2 and C_2H_2 were fitted with dual-site Langmuir-Freundlich isotherm model:[4]

$$q = q_{A,sat}\frac{b_A p^{\nu_A}}{1+b_A p^{\nu_A}} + q_{B,sat}\frac{b_B p^{\nu_B}}{1+b_B p^{\nu_B}} \qquad (1)$$

With T-dependent parameters *b*:

$$b = b_0 \exp\left(\frac{E}{RT}\right) \qquad (2)$$

The adsorption selectivity for CO_2/C_2H_2 separation is defined by:

$$S_{ads} = \frac{q_1/q_2}{p_1/p_2} \qquad (3)$$

Where q_1 and q_2 are the molar loadings in the adsorbed phase in equilibrium with the bulk gas phase with partial pressures p_1 and p_2.

Isosteric heat of adsorption calculations

A virial-type expression comprising the temperature-independent parameter a_i and b_j was employed to calculate the heat of adsorption for different gases (at different temperatures). In each case, the data were fitted using the equation:[5]

$$\ln P = \ln N + 1/T\sum_{i=0}^{m} a_i N^i + \sum_{j=0}^{n} b_j N^j \qquad (4)$$

Here, P is the pressure expressed in Pa, N is the amount adsorbed in mmol g^{-1}, T is the temperature in K, a_i and b_j are virial coefficients, and m, n represent the number of coefficients required to adequately describe the isotherms.

The values of the virial coefficients a_0 through a_m were then used to calculate the isosteric heat of adsorption using the following expression:

$$Q_{st} = -R\sum_{i=0}^{m} a_i N^j \qquad (5)$$

Q_{st} is the coverage-dependent isosteric heat of adsorption and R is the universal gas constant.

Supplementary Figures

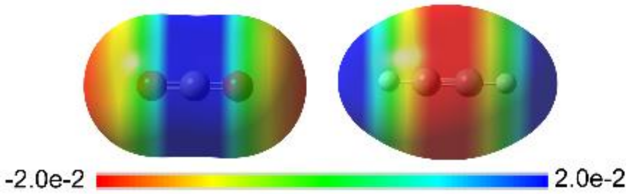

Dinymic diamater (Å)	3.3	3.3
Dimension (Å^3)	3.2 x 3.3 x 5.4	3.3 x 3.3 x 5.7
Boiling point (K)	194.7	189.3
Quadrupole moments (x10^{-40}C m^2)	-13.4	+20.5

Figure S1. Physical-chemical properties of CO_2 and C_2H_2.

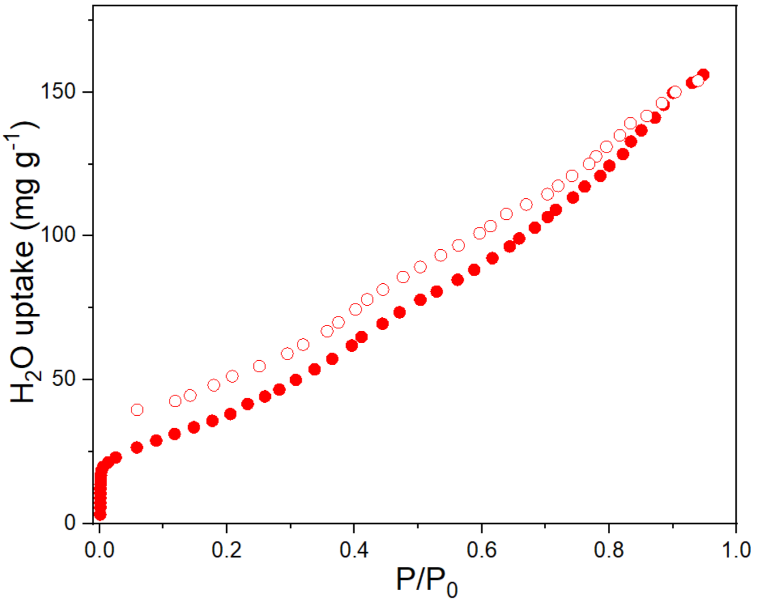

Figure S2. H_2O sorption isotherm of Ce(IV)-MIL-140-4F at 298 K.

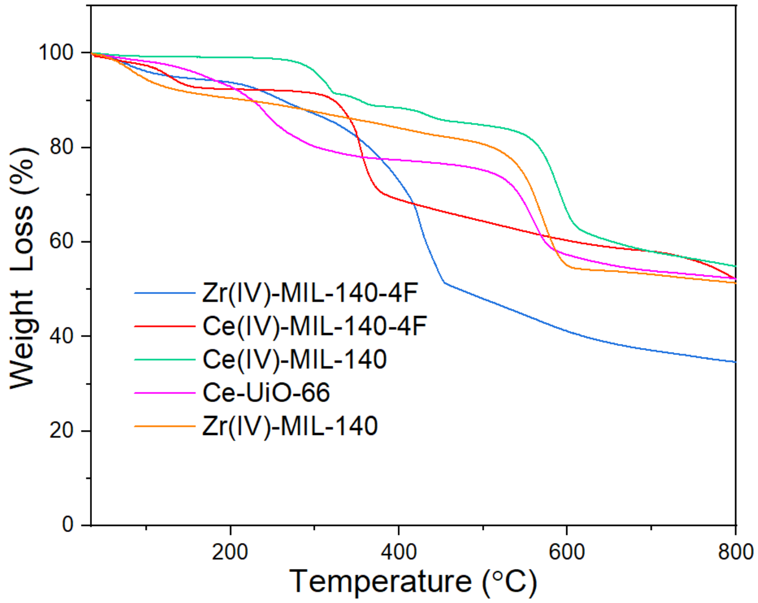

Figure S3. TGA curves of various materials collected with a heating rate of 10 K min^{-1} and an N_2 flow rate of 50 mL min^{-1}.

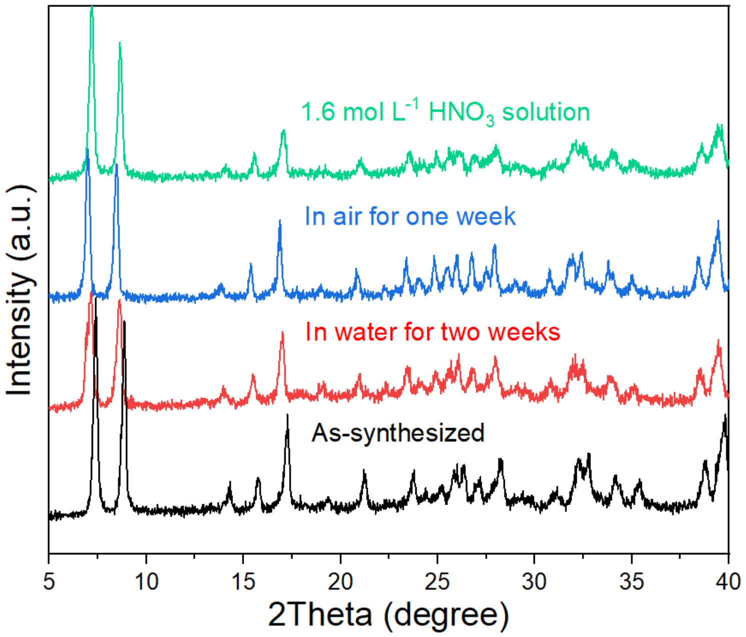

Figure S4. Experimental PXRD patterns of Ce(IV)-MIL-140-4F before and after disposition under various conditions.

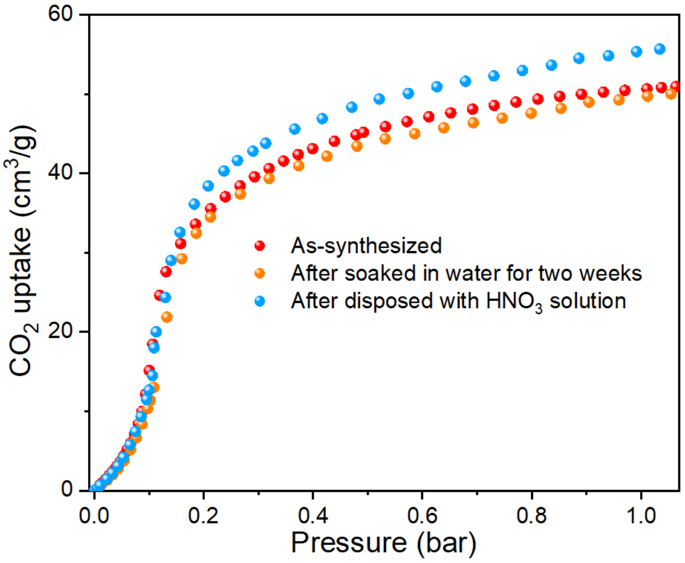

Figure S5. CO$_2$ sorption isotherms on Ce(IV)-MIL-140-4F after different treatments at 298 K.

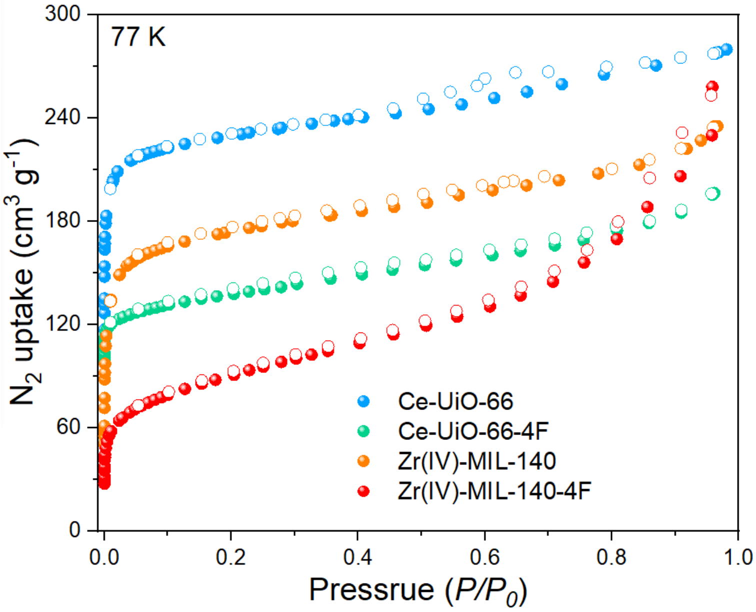

Figure S6. N_2 sorption isotherms of various materials collected at 77 K.

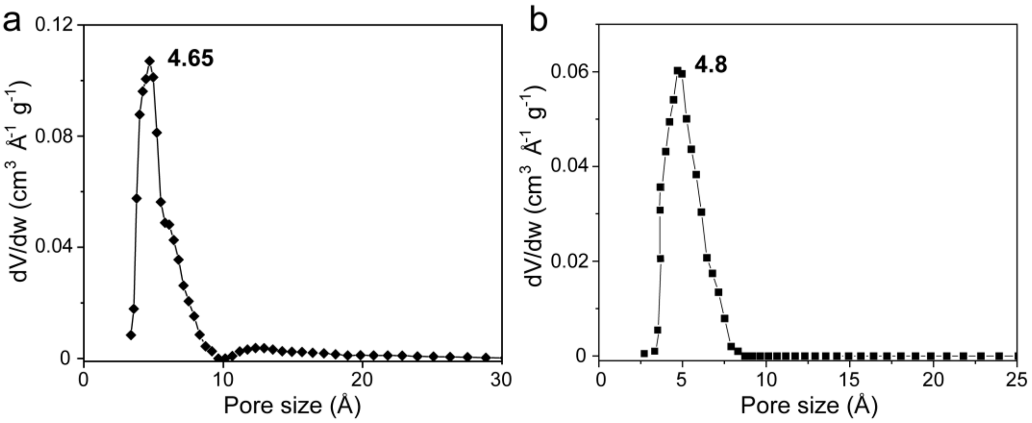

Figure S7. Pore size distributions of Ce(IV)-MIL-140-4F (a) and Zr(IV)-MIL-140-4F (b) derived from N_2 isotherms at 77 K.

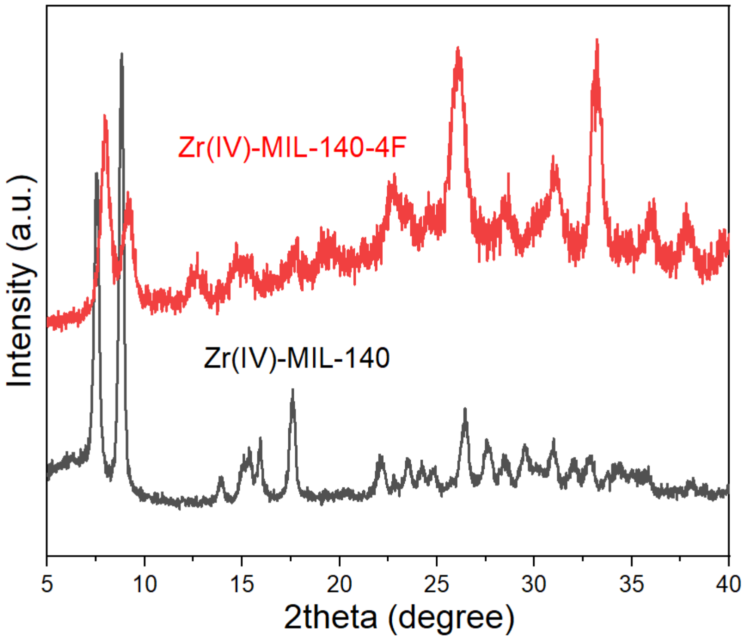

Figure S8. PXRD patterns of Zr(IV)-MIL-140-4F and Zr(IV)-MIL-140.

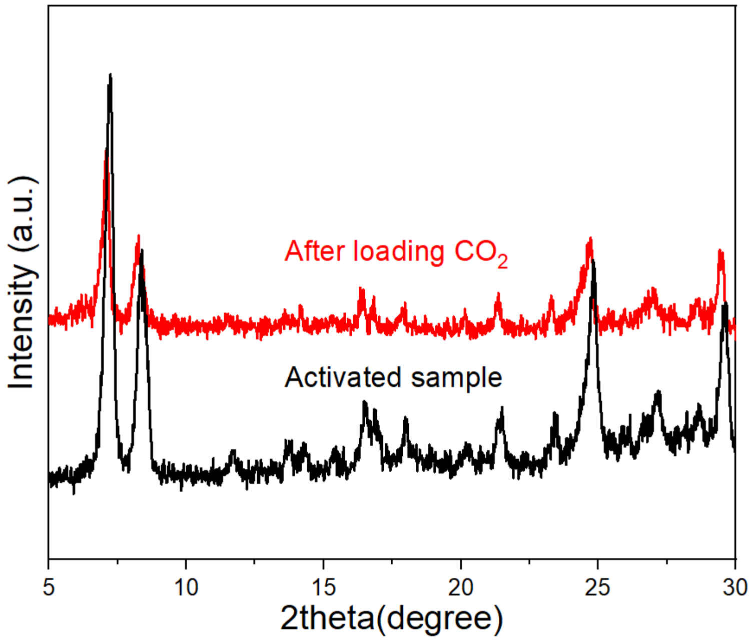

Figure S9. PXRD patterns of activated and CO_2-loaded Ce-UiO-66-4F.

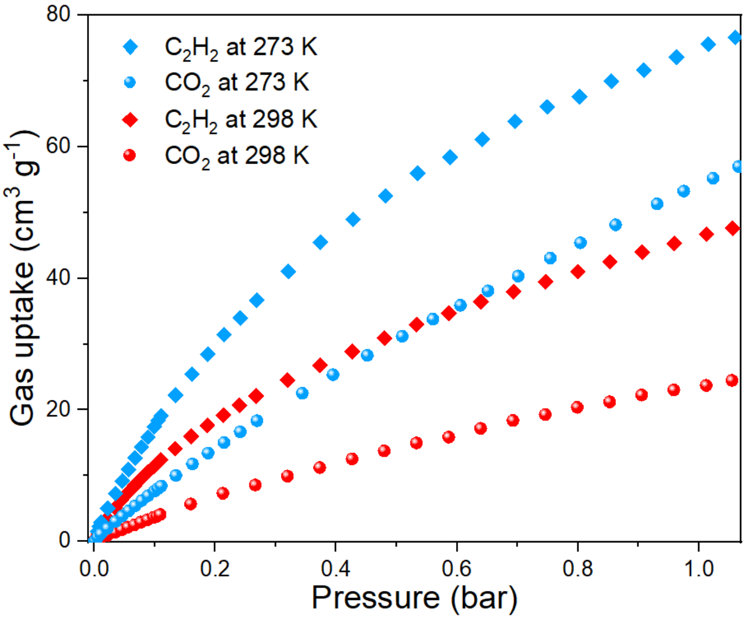

Figure S10. CO_2 and C_2H_2 adsorption isotherms of Zr(IV)-MIL-140-4F collected at 273 and 298 K.

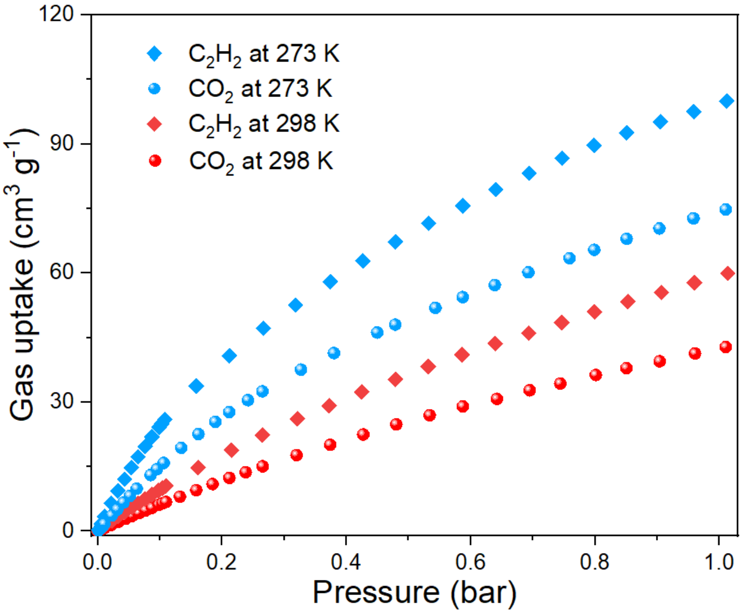

Figure S11. CO_2 and C_2H_2 adsorption isotherms of Ce-UiO-66 collected at 273 and 298 K.

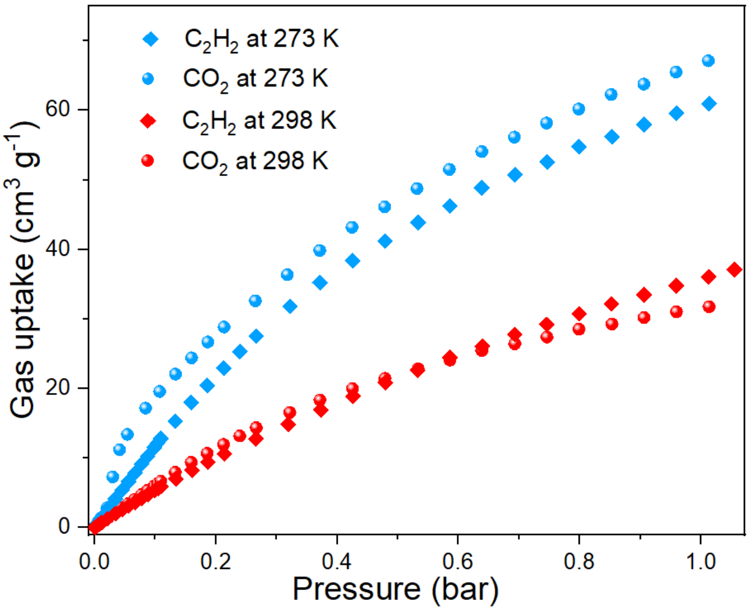

Figure S12. CO_2 and C_2H_2 adsorption isotherms of Ce-UiO-66-4F collected at 273 and 298 K.

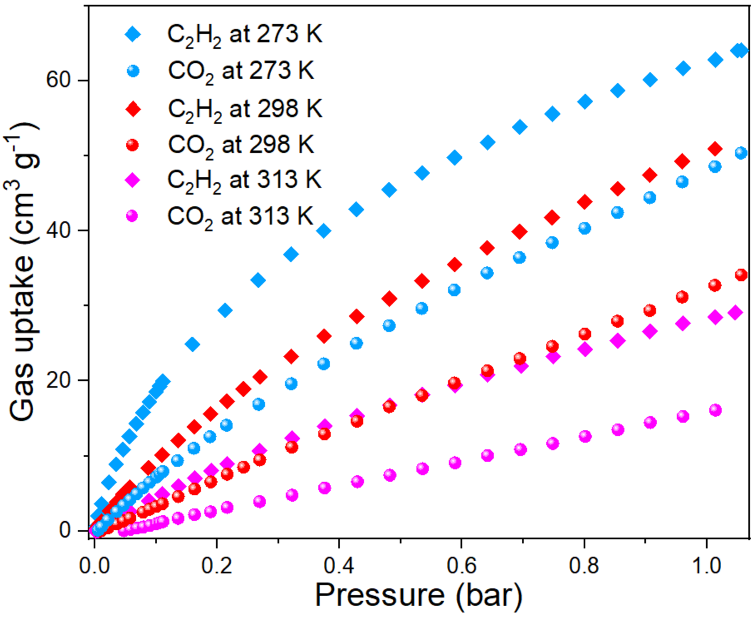

Figure S13. CO_2 and C_2H_2 adsorption isotherms of Zr-UiO-66-4F collected at 273, 298, and 313 K.

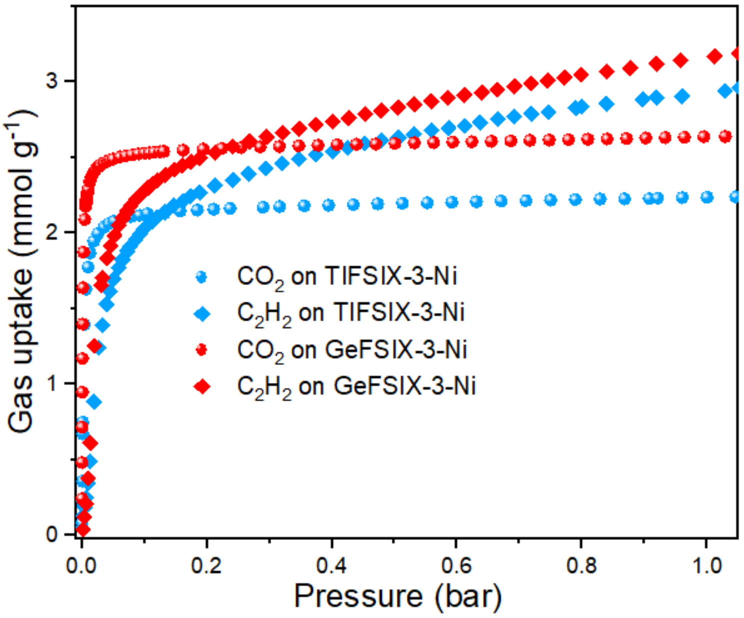

Figure S14. CO_2 and C_2H_2 adsorption isotherms of TIFSIX-3-Ni and GeFSIX-3-Ni at 298 K.

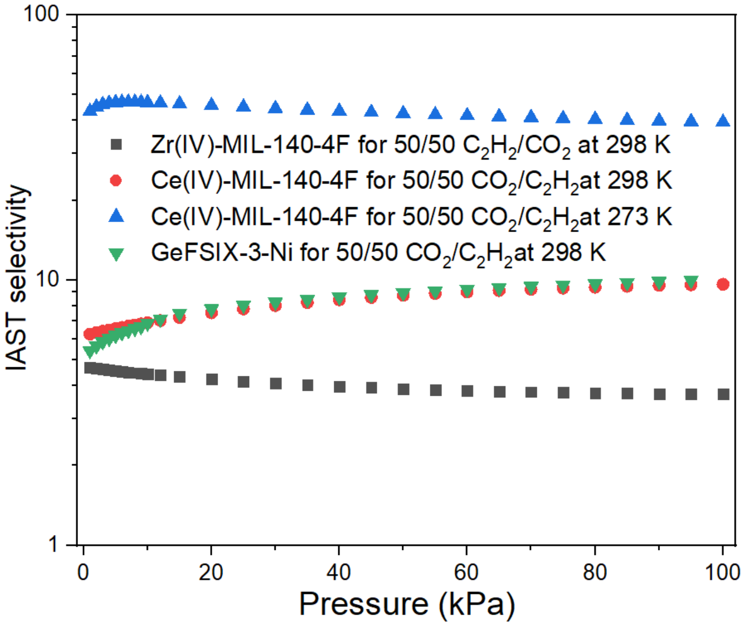

Figure S15. IAST adsorption selectivity for equimolar C_2H_2/CO_2 mixture of Ce(IV)/Zr(IV)-MIL-140-4F, and GeFSIX-3-Ni.

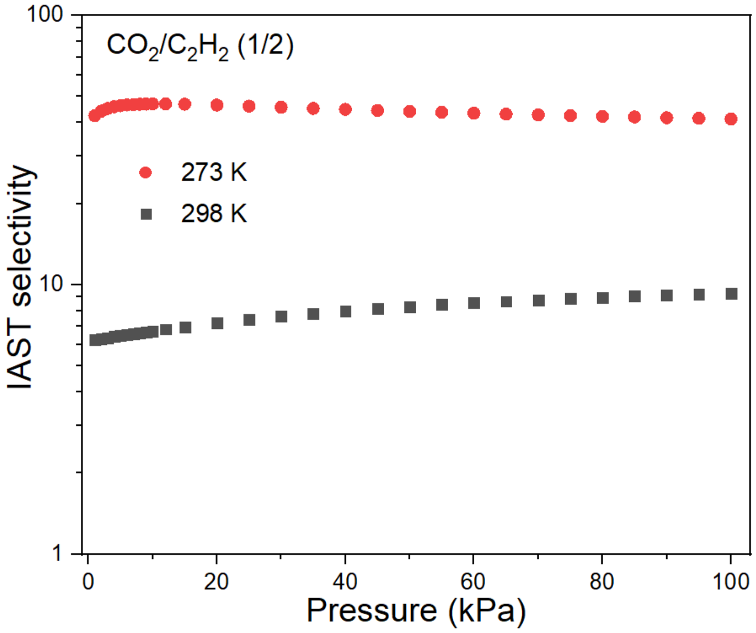

Figure S16. IAST adsorption selectivity for CO_2/C_2H_2 (1/2) mixture of Ce(IV)-MIL-140-4F.

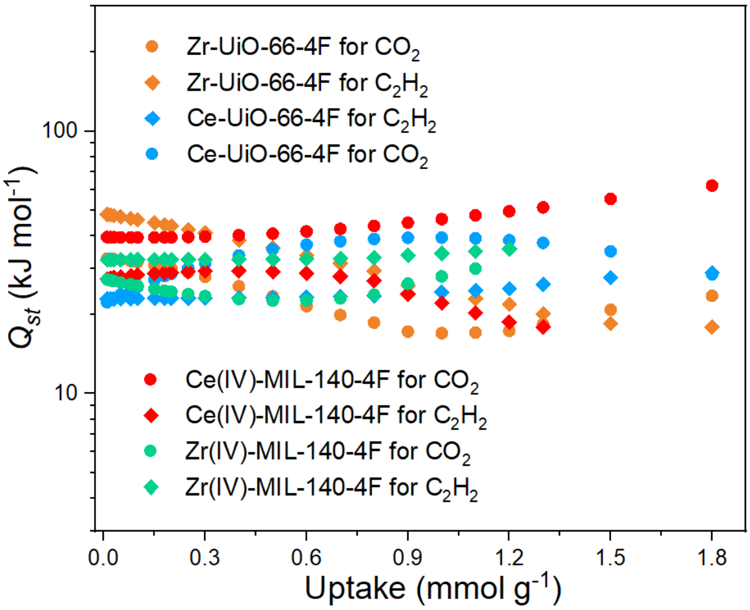

Figure S17. Heats of adsorption for C_2H_2 and CO_2 of different materials.

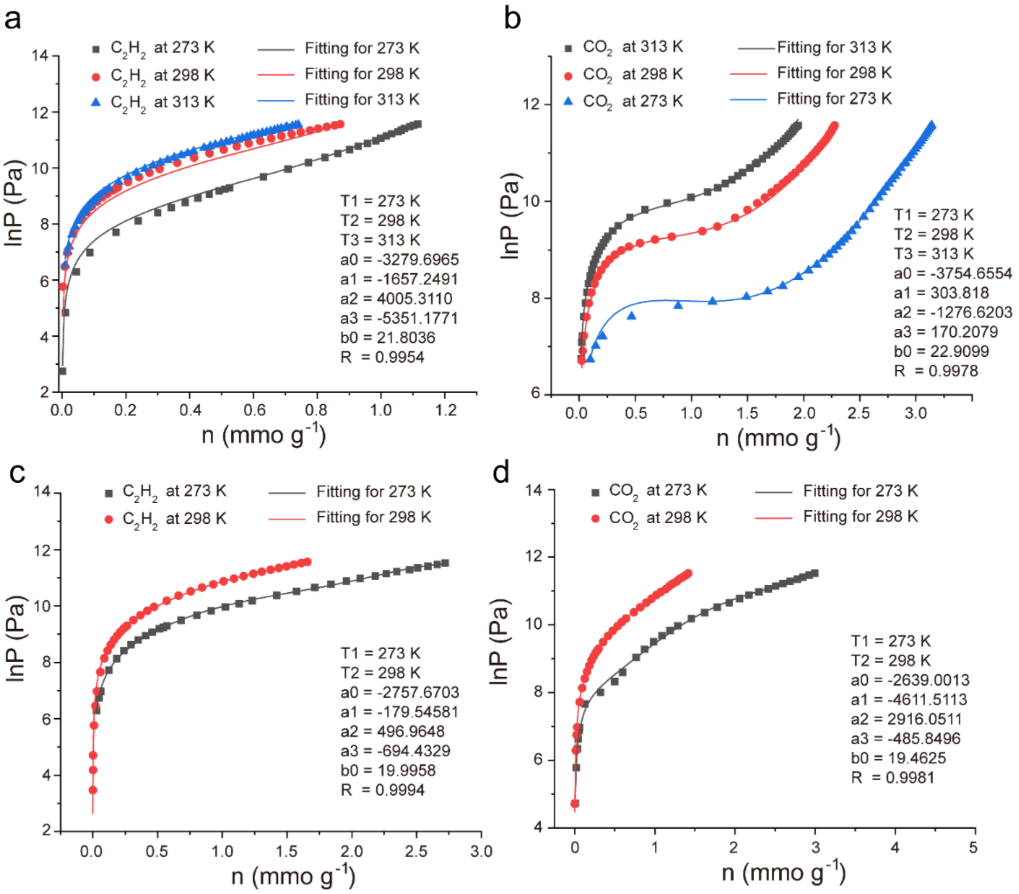

Figure S18. The virial fitting of C_2H_2 and CO_2 sorption isotherms for Ce(IV)-MIL-140-4F (a and b) and Ce-UiO-66-4F (c and d).

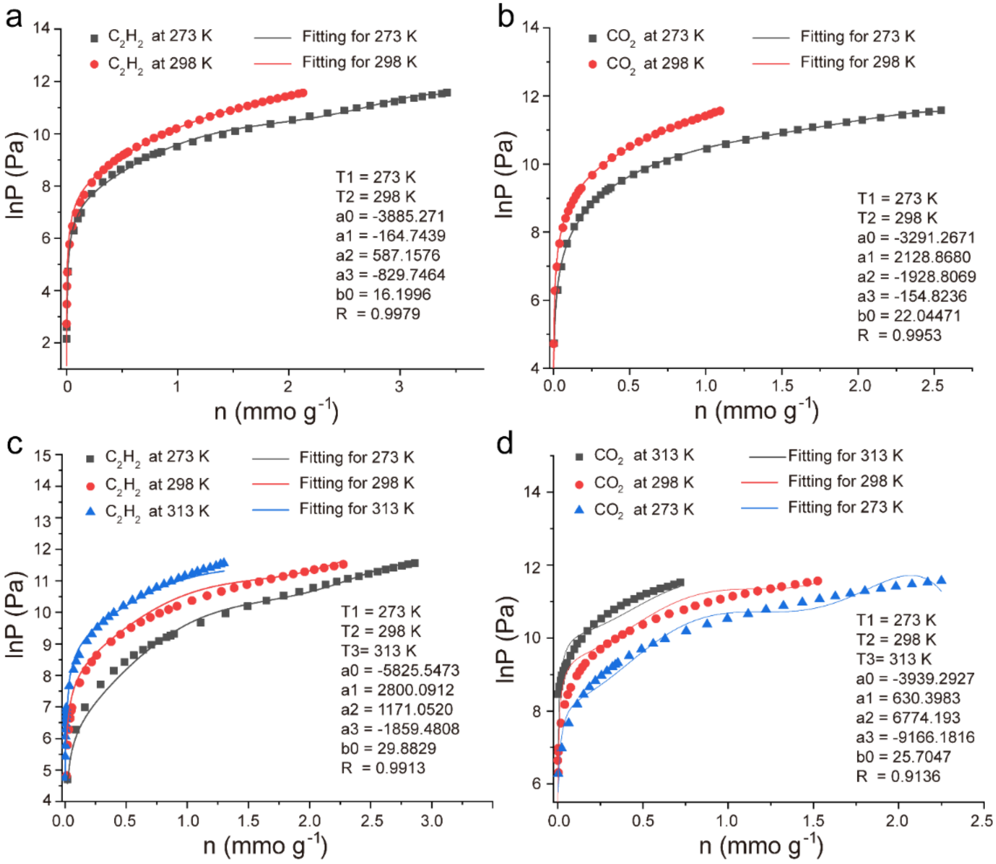

Figure S19. The virial fitting of C_2H_2 and CO_2 sorption isotherms for Zr(IV)-MIL-140-4F (a and b) and Zr-UiO-66-4F (c and d).

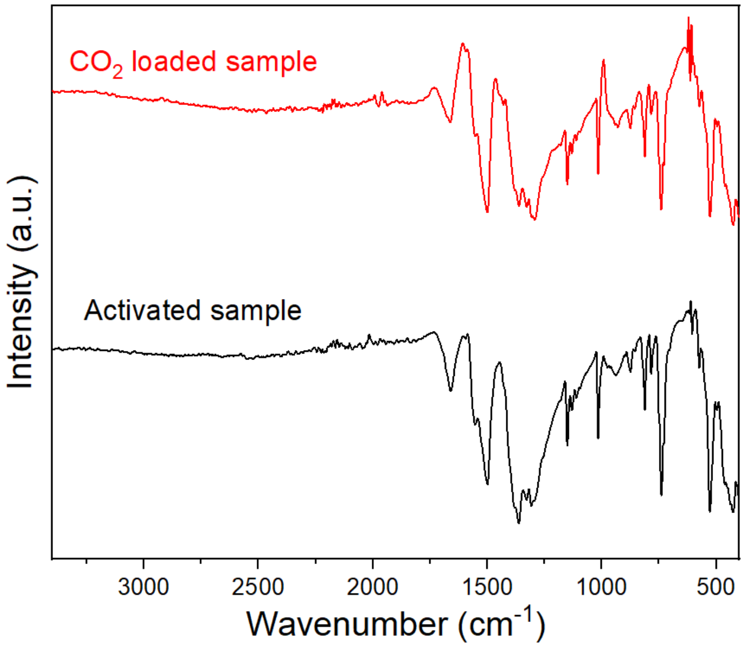

Figure S20. In situ FTIR spectra of activated and CO_2-loaded Ce(IV)-MIL-140.

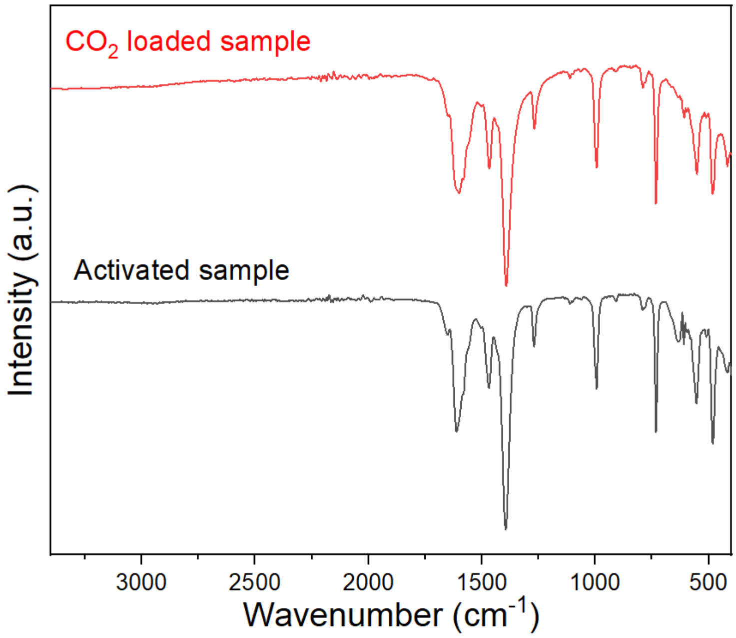

Figure S21. In situ FTIR spectra of activated and CO_2-loaded Ce-UiO-66-4F.

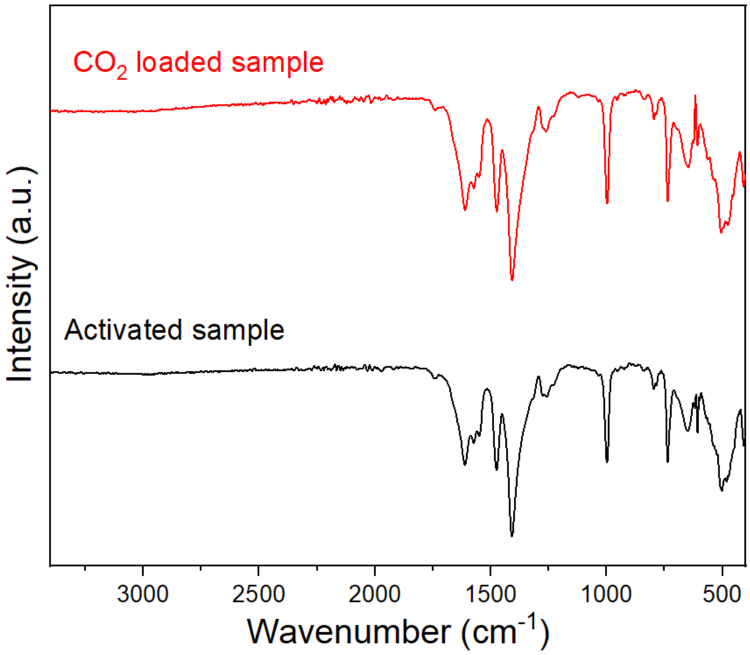

Figure S22. In situ FTIR spectra of activated and CO_2-loaded Zr(IV)-MIL-140-4F.

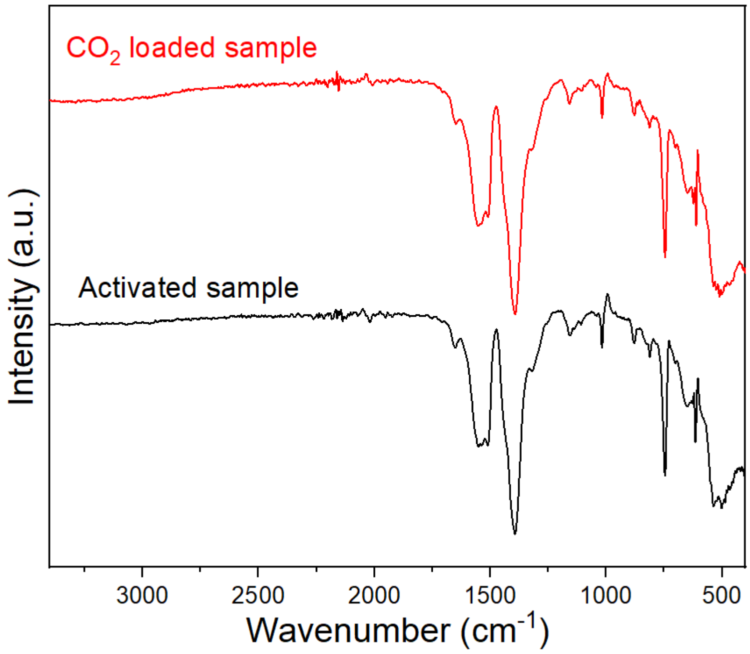

Figure S23. In situ FTIR spectra of activated and CO_2-loaded Zr(IV)-MIL-140.

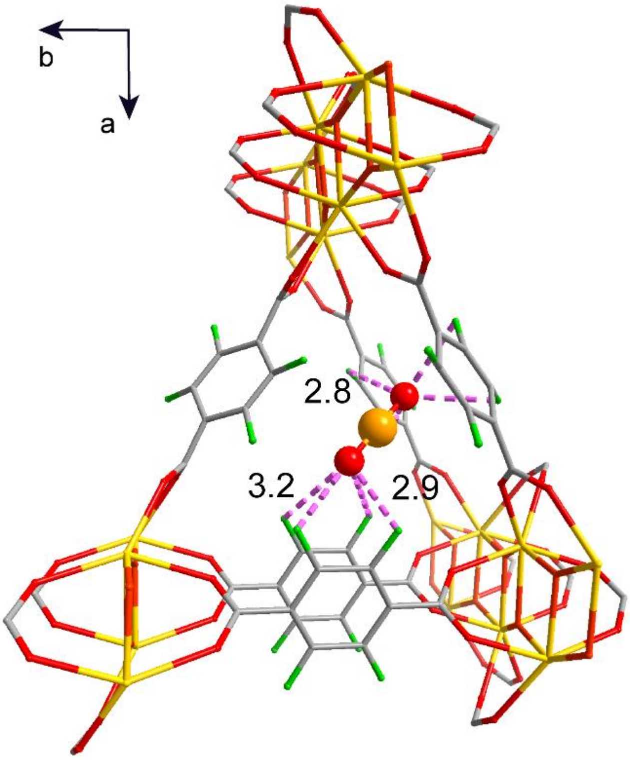

Figure S24. DFT-calculated configuration of CO_2 in the pore channel of Zr(IV)-MIL-140-4F.

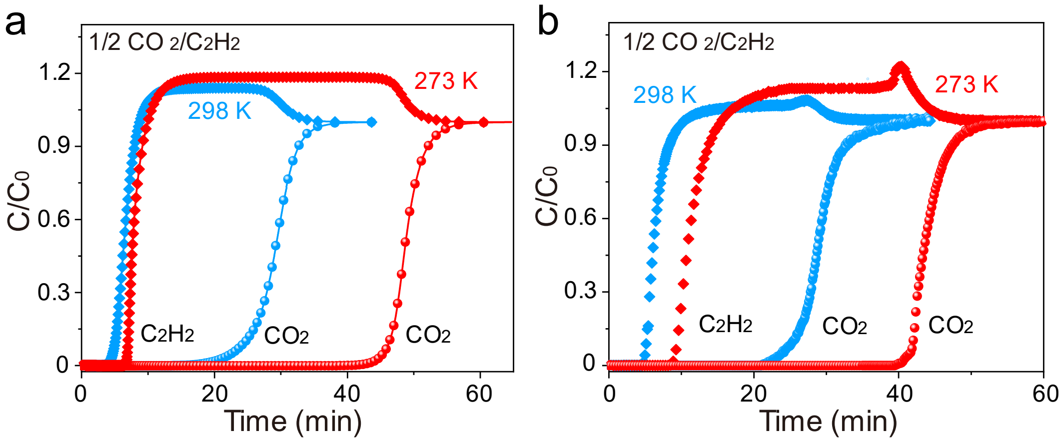

Figure S25. Simulated (a) and experimental (b) breakthrough curves for CO_2/C_2H_2 (1/2) mixture on Ce(IV)-MIL-140-4F at 273 and 298 K. **Note:** All the simulated and experimental breakthrough curves were investigated at 1 bar with a flow rate of 2 mL min^{-1}.

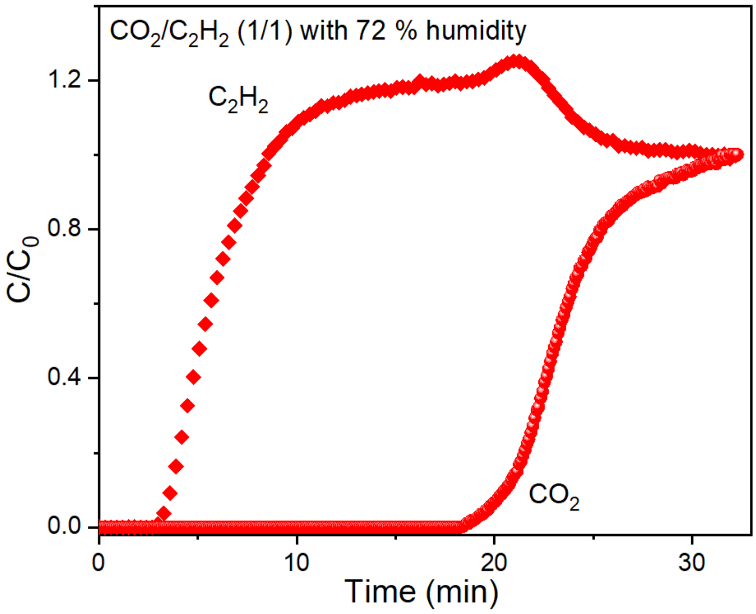

Figure S26. Breakthrough curves for CO_2/C_2H_2 (1/1) mixture on Ce(IV)-MIL-140-4F with 72% humidity at 298 K with a flow rate of 2 mL min^{-1}.

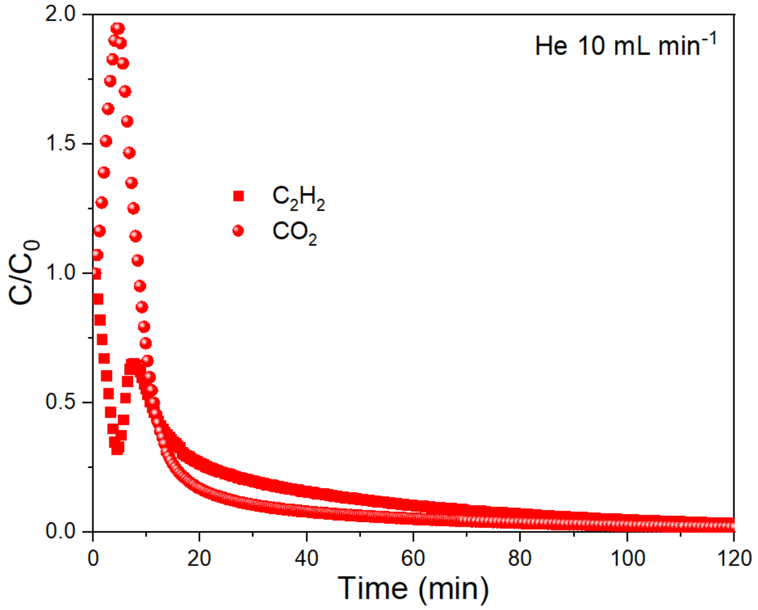

Figure S27. Desorption curves of C_2H_2 and CO_2 from Ce(IV)-MIL-140-4F-packed column collected by purging He with a flow rate of 10 mL min^{-1} at 298 K.

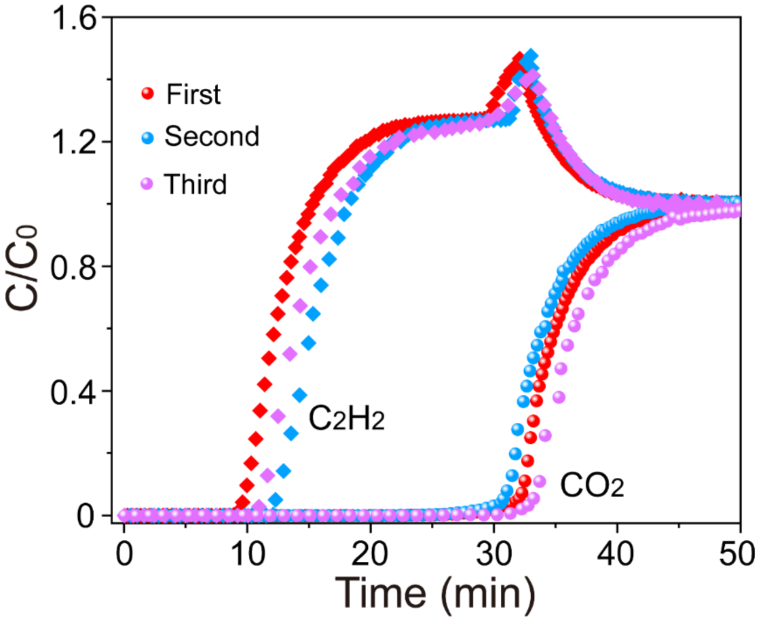

Figure S28. Multiple-cycle breakthrough tests of Ce(IV)-MIL-140-4F for CO_2/C_2H_2 (1/1) separation at 273 K.

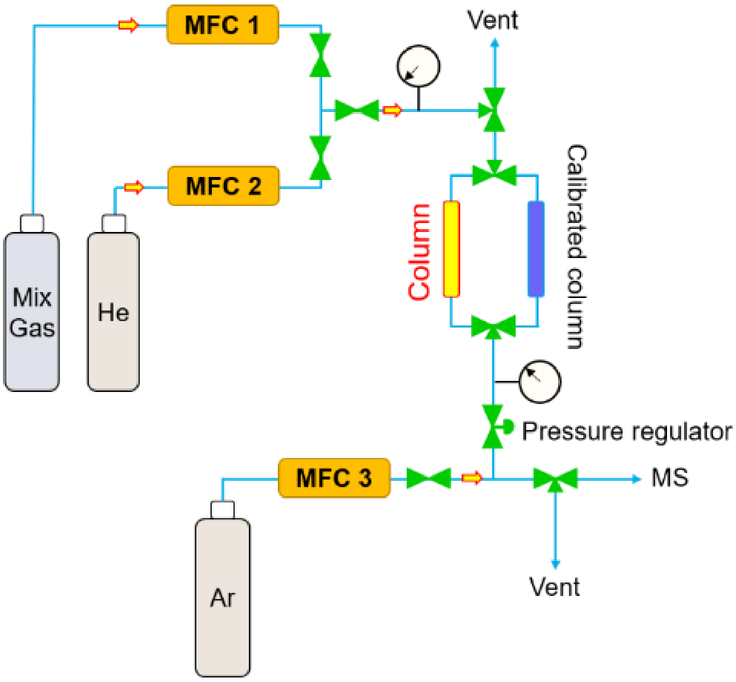

Figure S29. Schematic illustration of the breakthrough setup used in this study.

Supplementary Tables

Table S1. Crystallographic parameters and refinement details of Zr(IV)-MIL-140-4F.

	Zr(IV)-MIL-140-4F
Refinement method	Pawley
Empirical formula	ZrO5C8F4
Formula weight	243.3
Wavelength/Å	1.54056
Crystal system	monoclinic
Space group	*C2/c*
a (Å)	25.8173
b (Å)	11.6115
c (Å)	8.0821
β (º)	96.0813
V (Å3)	2253
Z	8
Calc. density/g cm^{-3}	2.051
R_p	3.3%
R_{wp}	5.4%
GOF	2.1

Table S2. Dual-site Langmuir-Freundlich parameter fits for CO_2 and C_2H_2 of different materials.

		Site A			Site B		
		$q_{A,sat}$	b_A	v_A	$q_{B,sat}$	b_B	v_B
		mol kg^{-1}	Pa^{-vA}		mol kg^{-1}	Pa^{-vB}	
Ce(IV)-MIL-140-4F	CO_2	1.7	5.737E-05	1	1.7	1.585E-18	5.2
(273 K)	C_2H_2	1.2	6.892E-05	1	0.7	6.283E-07	1
Ce(IV)-MIL-140-4F	CO_2	1.6	2.025E-05	1	1.2	2.104E-19	4.6
(298 K)	C_2H_2	0.35	3.904E-06	1	1.4	1.138E-05	1
GeFSIX-3-Ni	CO_2	1.16	3	1	2.50	1.098	1
(298 K)	C_2H_2	1.54	28.99	1	1.54	28.99	1
Zr(IV)-MIL-140-4F	CO_2	1.2	7.493E-06	1	1.2	7.493E-06	1
(298 K)	C_2H_2	5	3.744E-06	1	0.8	7.301E-05	1

Table S3. List of atomic positions for CO_2-loaded Ce(IV)-MIL-140-4F.

Atom	a	b	c	U (eq)
C1	0.21666	0.27477	0.59764	0.025
C2	0.25809	0.34506	0.61261	0.025
C3	0.29651	0.31875	0.51096	0.025
F4	0.2704	0.40359	0.75302	0.025
F5	0.18123	0.28209	0.70617	0.025
C6	0.34785	0.37146	0.54282	0.025
O7	0.36536	0.3869	0.6894	0.025
O8	0.36626	0.4254	0.43171	0.025
C9	0.95614	0.4572	0.21181	0.025
C10	0.95618	0.5757	0.21091	0.025
F11	0.91256	0.6322	0.16657	0.025
F12	0.91446	0.40011	0.14508	0.025
O13	0.03112	0.81314	0.17175	0.025
O14	0.03222	0.21566	0.17578	0.025
Ce15	0.55918	0.51436	0.16321	0.02352
O16	0.46273	0.49221	0.58686	0.025
C17	0.71702	0.77586	0.60805	0.025
C18	0.75845	0.84615	0.62301	0.025
C19	0.79688	0.81984	0.52136	0.025
F20	0.77076	0.90468	0.76343	0.025
F21	0.68159	0.78318	0.71658	0.025
C22	0.84821	0.87255	0.55323	0.025
O23	0.86573	0.88799	0.69981	0.025
O24	0.86663	0.92649	0.44212	0.025
C25	0.45578	0.95608	0.1997	0.025
C26	0.45582	0.07461	0.2005	0.025

F27	0.4122	0.13111	0.15616	0.025
F28	0.4141	0.89899	0.13298	0.025
O29	0.53148	0.31427	0.18385	0.025
O30	0.53258	0.71676	0.18619	0.025
Ce31	0.05882	0.01327	0.1528	0.02352
O32	0.9631	0.9933	0.59727	0.025
C33	0.78407	0.27603	0.91898	0.025
C34	0.74264	0.34613	0.90378	0.025
C35	0.70421	0.31965	1.00552	0.025
F36	0.73033	0.4046	0.76317	0.025
F37	0.81949	0.28351	0.81043	0.025
C38	0.65287	0.37213	0.97348	0.025
O39	0.63536	0.38749	0.82684	0.025
O40	0.63446	0.42599	0.08771	0.025
C41	0.04458	0.45518	0.30751	0.025
C42	0.04454	0.57368	0.30801	0.025
F43	0.08816	0.63038	0.35215	0.025
F44	0.08626	0.39828	0.37443	0.025
O45	0.9696	0.81522	0.34635	0.025
O46	0.9685	0.21774	0.34435	0.025
Ce47	0.44154	0.5141	0.35591	0.02352
O48	0.53799	0.49238	0.92902	0.025
C49	0.28371	0.7749	0.90687	0.025
C50	0.24228	0.84501	0.89167	0.025
C51	0.20385	0.81853	0.99341	0.025
F52	0.22997	0.90348	0.75106	0.025
F53	0.31913	0.78238	0.79832	0.025
C54	0.15251	0.87101	0.96137	0.025
O55	0.135	0.88637	0.81473	0.025
O56	0.1341	0.92487	0.0756	0.025
C57	0.54494	0.95628	0.31792	0.025
C58	0.5449	0.0748	0.32011	0.025
F59	0.58853	0.1315	0.36425	0.025
F60	0.58662	0.89937	0.38483	0.025
O61	0.46924	0.31413	0.33594	0.025
O62	0.46814	0.71661	0.33225	0.025
Ce63	0.9419	0.01523	0.36802	0.02352
O64	0.03763	0.99125	0.91692	0.025
C65	0.78407	0.72741	0.41987	0.025
C66	0.74264	0.65712	0.4049	0.025
C67	0.70421	0.68344	0.50655	0.025
F68	0.73033	0.5986	0.26449	0.025
F69	0.81949	0.72009	0.31134	0.025
C70	0.65287	0.63073	0.47469	0.025
O71	0.63536	0.61529	0.32811	0.025
O72	0.63446	0.57679	0.5858	0.025
C73	0.04458	0.54498	0.8057	0.025
C74	0.04454	0.42648	0.8066	0.025
F75	0.08816	0.36998	0.85094	0.025
F76	0.08626	0.60207	0.87243	0.025
O77	0.9696	0.18904	0.84576	0.025
O78	0.9685	0.78652	0.84173	0.025
Ce79	0.44154	0.48782	0.8543	0.02352
O80	0.53799	0.50997	0.43065	0.025
C81	0.28371	0.22632	0.40946	0.025
C82	0.24228	0.15603	0.39449	0.025
C83	0.20385	0.18235	0.49615	0.025
F84	0.22997	0.09751	0.25408	0.025
F85	0.31913	0.219	0.30093	0.025
C86	0.15251	0.12963	0.46428	0.025
O87	0.135	0.1142	0.3177	0.025
O88	0.1341	0.07569	0.57539	0.025
C89	0.54494	0.04611	0.81781	0.025
C90	0.5449	0.92758	0.81701	0.025
F91	0.58853	0.87108	0.86134	0.025
F92	0.58662	0.1032	0.88453	0.025
O93	0.46924	0.68792	0.83366	0.025
O94	0.46814	0.28543	0.83132	0.025
Ce95	0.9419	0.98891	0.86471	0.02352
O96	0.03763	0.00888	0.42024	0.025

C97	0.21666	0.72616	0.09853	0.025
C98	0.25809	0.65605	0.11373	0.025
C99	0.29651	0.68253	0.01199	0.025
F100	0.2704	0.59758	0.25434	0.025
F101	0.18123	0.71868	0.20708	0.025
C102	0.34785	0.63005	0.04403	0.025
O103	0.36536	0.61469	0.19067	0.025
O104	0.36626	0.57619	0.9298	0.025
C105	0.95614	0.547	0.71	0.025
C106	0.95618	0.4285	0.7095	0.025
F107	0.91256	0.37181	0.66536	0.025
F108	0.91446	0.60391	0.64308	0.025
O109	0.03112	0.18696	0.67116	0.025
O110	0.03222	0.78445	0.67316	0.025
Ce111	0.55918	0.48808	0.6616	0.02352
O112	0.46273	0.50981	0.08848	0.025
C113	0.71702	0.22728	0.11063	0.025
C114	0.75845	0.15717	0.12584	0.025
C115	0.79688	0.18366	0.0241	0.025
F116	0.77076	0.0987	0.26645	0.025
F117	0.68159	0.2198	0.21919	0.025
C118	0.84821	0.13117	0.05614	0.025
O119	0.86573	0.11581	0.20278	0.025
O120	0.86663	0.07732	0.94191	0.025
C121	0.45578	0.04591	0.69959	0.025
C122	0.45582	0.92738	0.6974	0.025
F123	0.4122	0.87068	0.65325	0.025
F124	0.4141	0.10281	0.63267	0.025
O125	0.53148	0.68805	0.68156	0.025
O126	0.53258	0.28557	0.68526	0.025
Ce127	0.05882	0.98696	0.64949	0.02352
O128	0.9631	0.01093	0.10059	0.025
C129	0	0.39589	0.2485	0.025
C130	0	0.63288	0.2481	0.025
C131	0	0.75988	0.24788	0.025
C132	0	0.26899	0.24872	0.025
C133	0.50036	0.89698	0.25891	0.025
C134	0.50036	0.134	0.26021	0.025
C135	0.50036	0.261	0.25999	0.025
C136	0.50036	0.77008	0.25912	0.025
C137	0	0.60408	0.74649	0.025
C138	0	0.36709	0.7469	0.025
C139	0	0.24009	0.74711	0.025
C140	0	0.73098	0.74628	0.025
C141	0.50036	0.1052	0.7586	0.025
C142	0.50036	0.86818	0.7573	0.025
C143	0.50036	0.74118	0.75752	0.025
C144	0.50036	0.2321	0.75838	0.025
C145	0.73773	1.21098	-1.53743	0
O146	0.75418	1.28334	-1.3859	0
O147	0.72125	1.1387	-1.68902	0
C148	-0.23736	-0.29427	1.08027	0
O149	-0.21333	-0.35674	1.23348	0
O150	-0.26137	-0.23187	0.92697	0

Table S4. List of atomic positions for Zr(IV)-MIL-140-4F.

Atom	a	b	c	U (eq)
C1	0.21635	0.27834	0.58959	0.025
C2	0.25772	0.3493	0.6027	0.025
C3	0.29609	0.32369	0.49874	0.025
F4	0.27001	0.40799	0.74312	0.025
F5	0.18097	0.28503	0.70028	0.025
C6	0.34735	0.37726	0.52828	0.025
O7	0.36484	0.39299	0.67455	0.025
O8	0.36574	0.43147	0.41597	0.025
C9	0.95477	0.47366	0.16614	0.025
C10	0.95481	0.59205	0.16548	0.025
F11	0.91125	0.64773	0.12325	0.025
F12	0.91315	0.41588	0.10113	0.025

O13	0.03108	0.81294	0.17243	0.025
O14	0.03218	0.21603	0.17524	0.025
Zr15	0.55838	0.52376	0.13713	0.02352
O16	0.46207	0.49992	0.56703	0.025
O17	0.62825	0.35757	0.46479	0.025
C18	0.71599	0.78781	0.57627	0.025
C19	0.75736	0.85876	0.58938	0.025
C20	0.79574	0.83315	0.48541	0.025
F21	0.76965	0.91745	0.7298	0.025
F22	0.68062	0.79449	0.68695	0.025
C23	0.847	0.88672	0.51495	0.025
O24	0.86449	0.90245	0.66122	0.025
O25	0.86539	0.94093	0.40264	0.025
C26	0.45513	0.96324	0.17975	0.025
C27	0.45517	0.08258	0.1788	0.025
F28	0.41161	0.13826	0.13658	0.025
F29	0.41351	0.90547	0.11473	0.025
O30	0.53072	0.32336	0.15883	0.025
O31	0.53182	0.7255	0.16191	0.025
Zr32	0.05874	0.0143	0.15046	0.02352
O33	0.96172	1.00939	0.5537	0.025
O34	0.12861	0.84715	0.47839	0.025
C35	0.78294	0.28961	0.884	0.025
C36	0.74157	0.35892	0.87093	0.025
C37	0.7032	0.33178	0.97489	0.025
F38	0.72928	0.41712	0.73055	0.025
F39	0.81832	0.29771	0.77333	0.025
C40	0.65194	0.38331	0.94538	0.025
O41	0.63445	0.39835	0.79911	0.025
O42	0.63355	0.4368	0.05746	0.025
C43	0.04452	0.45555	0.3073	0.025
C44	0.04448	0.57394	0.30804	0.025
F45	0.08804	0.63135	0.35029	0.025
F46	0.08614	0.39943	0.37228	0.025
O47	0.96821	0.83159	0.30121	0.025
O48	0.96711	0.23463	0.29808	0.025
Zr49	0.44091	0.52142	0.33635	0.02352
O50	0.53722	0.50142	0.90669	0.025
O51	0.37104	0.35245	0.0086	0.025
C52	0.2833	0.7792	0.89761	0.025
C53	0.24193	0.84851	0.88454	0.025
C54	0.20356	0.82137	0.98849	0.025
F55	0.22964	0.90671	0.74415	0.025
F56	0.31867	0.7873	0.78693	0.025
C57	0.15229	0.8729	0.95898	0.025
O58	0.1348	0.88794	0.81272	0.025
O59	0.13391	0.92638	0.07106	0.025
C60	0.54416	0.96502	0.29398	0.025
C61	0.54412	0.08435	0.29443	0.025
F62	0.58768	0.14177	0.33669	0.025
F63	0.58578	0.9089	0.35895	0.025
O64	0.46857	0.32212	0.31454	0.025
O65	0.46747	0.72422	0.31168	0.025
Zr66	0.94055	0.03184	0.32275	0.02352
O67	0.03757	0.991	0.92029	0.025
O68	0.87068	0.86191	-0.00473	0.025
C69	0.78294	0.74058	0.384	0.025
C70	0.74157	0.66963	0.37089	0.025
C71	0.7032	0.69524	0.47486	0.025
F72	0.72928	0.61094	0.23047	0.025
F73	0.81832	0.73389	0.27332	0.025
C74	0.65194	0.64167	0.44532	0.025
O75	0.63445	0.62594	0.29905	0.025
O76	0.63355	0.58745	0.55763	0.025
C77	0.04452	0.54527	0.80745	0.025
C78	0.04448	0.42688	0.80812	0.025
F79	0.08804	0.3712	0.85034	0.025
F80	0.08614	0.60304	0.87246	0.025
O81	0.96821	0.20598	0.80117	0.025
O82	0.96711	0.80289	0.79836	0.025

Zr83	0.44091	0.49517	0.83647	0.02352
O84	0.53722	0.519	0.40657	0.025
O85	0.37104	0.66136	0.50881	0.025
C86	0.2833	0.23112	0.39733	0.025
C87	0.24193	0.16016	0.38422	0.025
C88	0.20356	0.18578	0.48819	0.025
F89	0.22964	0.10148	0.2438	0.025
F90	0.31867	0.22443	0.28665	0.025
C91	0.15229	0.13221	0.45865	0.025
O92	0.1348	0.11647	0.31238	0.025
O93	0.13391	0.07799	0.57096	0.025
C94	0.54416	0.05568	0.79385	0.025
C95	0.54412	0.93634	0.79479	0.025
F96	0.58768	0.88066	0.83702	0.025
F97	0.58578	0.11345	0.85886	0.025
O98	0.46857	0.69557	0.81477	0.025
O99	0.46747	0.29343	0.81169	0.025
Zr100	0.94055	1.00463	0.82314	0.02352
O101	0.03757	0.00954	0.4199	0.025
O102	0.87068	0.17177	0.49521	0.025
C103	0.21635	0.72931	0.08959	0.025
C104	0.25772	0.66	0.10266	0.025
C105	0.29609	0.68714	-0.00129	0.025
F106	0.27001	0.6018	0.24305	0.025
F107	0.18097	0.72122	0.20027	0.025
C108	0.34735	0.63561	0.02822	0.025
O109	0.36484	0.62057	0.17448	0.025
O110	0.36574	0.58213	0.91613	0.025
C111	0.95477	0.56337	0.66629	0.025
C112	0.95481	0.44499	0.66556	0.025
F113	0.91125	0.38757	0.62331	0.025
F114	0.91315	0.61949	0.60131	0.025
O115	0.03108	0.18734	0.67238	0.025
O116	0.03218	0.78429	0.67552	0.025
Zr117	0.55838	0.4975	0.63725	0.02352
O118	0.46207	0.51751	0.06691	0.025
O119	0.62825	0.66647	0.965	0.025
C120	0.71599	0.23973	0.07599	0.025
C121	0.75736	0.17042	0.08906	0.025
C122	0.79574	0.19755	-0.01489	0.025
F123	0.76965	0.11222	0.22945	0.025
F124	0.68062	0.23163	0.18667	0.025
C125	0.847	0.14602	0.01462	0.025
O126	0.86449	0.13099	0.16088	0.025
O127	0.86539	0.09254	0.90253	0.025
C128	0.45513	0.05391	0.67962	0.025
C129	0.45517	0.93457	0.67916	0.025
F130	0.41161	0.87716	0.63691	0.025
F131	0.41351	0.11003	0.61464	0.025
O132	0.53072	0.6968	0.65906	0.025
O133	0.53182	0.29471	0.66192	0.025
Zr134	0.05874	0.98709	0.65085	0.02352
O135	0.96172	0.02792	0.05331	0.025
O136	0.12861	0.15701	0.97832	0.025
C137	0	0.39552	0.25017	0.025
C138	0	0.6323	0.25024	0.025
C139	0	0.75918	0.25027	0.025
C140	0	0.26874	0.25014	0.025
C141	0.49965	0.90499	0.23684	0.025
C142	0.49965	0.14271	0.23663	0.025
C143	0.49965	0.26959	0.23667	0.025
C144	0.49965	0.77821	0.23681	0.025
C145	0	0.60353	0.75035	0.025
C146	0	0.36675	0.75029	0.025
C147	0	0.23987	0.75025	0.025
C148	0	0.7303	0.75039	0.025
C149	0.49965	0.11394	0.73675	0.025
C150	0.49965	0.87621	0.73696	0.025
C151	0.49965	0.74933	0.73693	0.025
C152	0.49965	0.24072	0.73679	0.025

Supplementary Movie Titles

Movie S1. Development of CO_2 and C_2H_2 concentration along the length of the fixed bed of Ce(IV)-MIL-140-4F at 273 K.
Movie S2. Development of CO_2 and C_2H_2 concentration along the length of the fixed bed of Ce(IV)-MIL-140-4F at 298 K.
Movie S3. Development of gas phase concentration along the length of the fixed bed of Zr(IV)-MIL-140-4F at 298 K.

References

[1] R. D'Amato, A. Donnadio, M. Carta, C. Sangregorio, D. Tiana, R. Vivani, M. Taddei, F. Costantino, *ACS Sustainable Chem. Eng.* **2018**, *7*, 394-402.
[2] a) R. Krishna, *RSC Adv.* **2017**, *7*, 35724-35737; b) R. Krishna, *RSC Adv.* **2015**, *5*, 52269-52295; c) R. Krishna, *Microporous Mesoporous Mater.* **2014**, *185*, 30-50; dR. Krishna, *Phys. Chem. Chem. Phys.* **2016**, *18*, 15482-15495.
[3] Z. Zhang, Q. Yang, X. Cui, L. Yang, Z. Bao, Q. Ren, H. Xing, *Angew. Chem. Int. Ed.* **2017**, *56*, 16282-16287.
[4] a) K. S. Walton, D. S. Sholl, *AIChE J.* **2015**, *61*, 2757-2762; b) A. L. Myers, J. M. Prausnitz, *AIChE J.* **1965**, *11*, 121-127.
[5] a) K. J. Chen, H. S. Scott, D. G. Madden, T. Pham, A. Kumar, A. Bajpai, M. Lusi, K. A. Forrest, B. Space, J. J. Perry, M. J. Zaworotko, *Chem* **2016**, *1*, 753-765; b) Z. Zhang, S. B. Peh, Y. Wang, C. Kang, W. Fan, D. Zhao, *Angew. Chem. Int. Ed.* **2020**, *59*, 18927-18932.